ROHM & HAAS COMPANY

REDSTONE ARSENAL RESEARCH DIVISION

HUNTSVILLE, ALABAMA

REPORT NO . P-62-27

QUARTERLY PROGRESS REPORT

ON ENGINEERING RESEARCH (U)

September 15, 1962 to December 15, 1962

ORDNANCE CORPS, DEPARTMENT OF THE ARMY
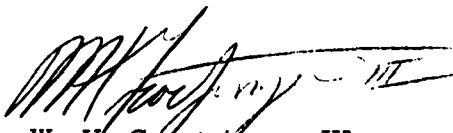
MAI 1 ᵔ ᵔᵔᵔ

INDIA

A

ROHM & HAAS COMPANY

REDSTONE ARSENAL RESEARCH DIVISION
HUNTSVILLE, ALABAMA

REPORT NO. P-62-27

QUARTERLY PROGRESS REPORT

ON ENGINEERING RESEARCH (U)

Approved:

W. H. Groetzinger, III
Head, Engineering Section

Contributing Staff:

Charles H. Parr

Orville H. Loeffler
General Manager

April 19, 1963

Work reported herein was carried
out under the following contract

DA-01-021-ORD-11878

FOREWORD

This report is one in a series of Quarterly Progress Reports issued by the Redstone Arsenal Research Division of Rohm & Haas Company. The complete list of reports, together with approximate issuance dates, is shown below.

Inorganic Chemistry	Process Research	Physical Chemistry	Engineering Research
Jan. 25	Feb. 25	March 25	Jan. 10
April 25	May 25	June 25	April 10
July 25	August 25	Sept. 25	July 10
Oct. 25	Nov. 25	Dec. 25	Oct. 10

Interior Ballistics	Chemical and Propellant Processing	A.R.P.A. Projects
Feb. 10	March 10	Jan. 15
May 10	June 10	April 15
August 10	Sept. 10	July 15
Nov. 10	Dec. 10	Oct. 15

The distribution of all reports is made according to the JANAF Mailing List plus approved supplements.

ROHM & HAAS COMPANY

REDSTONE ARSENAL RESEARCH DIVISION
HUNTSVILLE, ALABAMA

ABSTRACT

A numerical method of calculating deformations and stresses in an elastic solid propellant grain having a circular perforation and flat ends and bonded to a rigid motor case was used to calculate stresses and deformations caused by axial acceleration loading. Two grain end situations were considered: both ends free and one end free with the other bonded to the motor case. The dimensionless displacements of critical parts of the grain were calculated as functions of the inner-to-outer radius ratio α, the length-to-diameter ratio λ, and Poisson's ratio ν. The dimensionless radial and shear stresses at the propellant-motor case interface were also calculated as well as the percentage of total load carried by the bonded end for grains bonded on one end.

The equations of motion of a viscoelastic solid were reduced to a single Poisson equation by assuming that the displacements do not vary with the coordinate direction along which the acceleration is applied. A general solution to this equation was obtained for hollow cylinders of infinite length having generators parallel to the direction of acceleration and transverse cross sections with $p(p \neq 0)$ axes of symmetry. The solution was applied to solid propellant grains of infinite length having star-shaped internal perforations to determine the stresses and deformations caused by axial acceleration under the conditions of zero displacement at the outer boundary and zero surface stresses at the inner boundary.

TABLE OF CONTENTS

DEFORMATIONS AND STRESSES IN AXIALLY ACCELERATED CASE-BONDED SOLID PROPELLANT GRAINS OF FINITE LENGTH

Charles H. Parr

1. Introduction

A numerical method for calculating deformations and stresses in an elastic solid propellant grain of finite length having a circular perforation and flat ends and bonded to a rigid motor case was reported previously[1]. While the method considered internal pressure, shrinkage, and axial acceleration loads, the calculations presented were concerned primarily with shrinkage loads. Additional calculations using this method have been made for axial acceleration loads. Two end conditions were considered: two free ends, and one fixed and one free end. As pointed out previously, it is possible to present results in dimensionless form in terms of only three parameters: the inner-to-outer radius ratio α, the length-to-diameter ratio λ, and Poisson's ratio ν.

2. Correction to Previous Report

An incorrect statement was made on page 11 of Report P-61-17 concerning the state of stress at the midsection of a cylinder of finite length which is geometrically symmetrical about the midsection and loaded by axial acceleration. It was stated that the stress condition in the midsection plane was exactly the same as in an infinitely long cylinder. Actually, at this plane the radial displacement, normal stress, and normal strain are zero as in the infinite cylinder as will be shown below. The axial displacement and shear stress and shear strain at the midsection plane, however, cannot be evaluated from considerations of the midsection alone and must depend on other properties of the cylinder, specifically, the length.

---

[1]Rohm & Haas Company, Quarterly Progress Report on Engineering Research, No. P-61-17, June 1962.

Consider the accelerated cylinder in Fig. 1. If the acceleration is considered positive as shown, a negative acceleration must be equivalent to an acceleration in the opposite direction. Because linear analysis is used, a simple reversal of the signs of the stresses, strains, and displacement results if the direction of acceleration is changed. Consideration of this point leads to the conclusion that the radial displacement along the geometric line of symmetry m - m must be zero. If the radial displacement is zero, the radial and circumferential strains are zero along this line by definition.

To demonstrate that the axial strain is zero is more difficult. From the equation for radial displacement, Eq. 9 in Report P-61-17 (neglecting shrinkage terms), namely

$$u_\rho = \frac{[1+\nu]}{\rho} \left[\psi + [1-\nu]\phi \right] - \nu \rho \eta Z , \tag{9}$$

there results from setting the displacement equal to zero[1]

$$\psi + [1-\nu]\phi = \frac{\nu \rho^2 \eta Z}{1+\nu} . \tag{34}$$

The first and second derivatives of Eq. 34 are

$$\frac{\partial \psi}{\partial \rho} + [1-\nu]\frac{\partial \phi}{\partial \rho} = \frac{2\nu \rho \eta Z}{1+\nu} \tag{35}$$

and

$$\frac{\partial^2 \psi}{\partial \rho^2} + [1-\nu]\frac{\partial^2 \phi}{\partial \rho^2} = \frac{2\nu \eta Z}{1+\nu} . \tag{36}$$

Addition of the field equations given by Eqs. 7 and 8, namely

$$\frac{\partial^2 \phi}{\partial \rho^2} - \frac{1}{\rho}\frac{\partial \phi}{\partial \rho} + \frac{\partial^2 \phi}{\partial \eta^2} = 0 \tag{7}$$

---

[1]Equations are numbered consecutively with Report P-61-17.

and

$$\frac{\partial^2 \psi}{\partial \rho^2} - \frac{1}{\rho} \frac{\partial \psi}{\partial \rho} + \frac{\partial^2 \psi}{\partial \eta^2} = \frac{\partial^2 \phi}{\partial \eta^2} \quad , \tag{8}$$

and substitution of Eqs. 35 and 36 gives

$$\frac{\partial^2 \psi}{\partial \eta^2} = \nu \frac{\partial^2 \phi}{\partial \eta^2} \quad . \tag{37}$$

Because of the anti-symmetric quality of the radial displacement about m - m for the axial acceleration loading, it can also be concluded that

$$\frac{\partial^2 u_\rho}{\partial \eta^2} = 0 \tag{38}$$

along m - m, i.e., there is an inflection point in the radial displacement at m - m. Eqs. 37, 9, and 38 when combined result in

$$\frac{\partial^2 \phi}{\partial \eta^2} = \frac{\partial^2 \psi}{\partial \eta^2} = 0 \tag{39}$$

along m - m. Eqs. 7 and 8 now yield for the general form of ϕ and ψ along the line m - m

$$\phi = A \rho^2 + B \tag{40}$$

and

$$\psi = C \rho^2 + D \quad , \tag{41}$$

which can be evaluated with aid of the boundary conditions

$$u_\rho = u_\eta = 0 \quad \text{at } \rho = 1$$

and

$$\sigma_{\rho\eta} = \sigma_\rho = 0 \quad \text{at } \rho = \alpha$$

to give

$$\phi = \frac{\eta_0 Z}{2} \left[\frac{\alpha^2}{1-\nu} - \frac{\rho^2}{1+\nu} \right] \tag{42}$$

and

$$\psi = \frac{\eta_0 Z}{2} \left[\rho^2 - \alpha^2 \right] \quad , \tag{43}$$

where η_0 is the axial coordinate at m - m. By substituting Eq. 42 and 43 into the expression for axial strain, namely

$$\epsilon_\eta = -\frac{[1+\nu]}{\rho}\left[\frac{\partial\psi}{\partial\rho} + 2\frac{\partial\psi}{\partial\rho}\right] + \eta Z \quad , \tag{44}$$

the axial strain can be found to be zero along m - m. Thus the three normal strains, and hence also the three normal stresses, are zero at the midsection as well as the radial displacement.

Physical considerations similar to those made previously for the radial displacement will establish that under axial acceleration not only the radial displacement but all of the normal strains and stresses as well are anti-symmetric functions with respect to the midsection, while the axial displacement shear stress, and shear strain are symmetric functions. Thus, it is possible to deduce the complete solution of a cylinder which is geometrically similar with respect to the midsection by considering only half of the cylinder in the numerical solution, with resulting significant savings in time and cost.

3. Alternative Method for Obtaining Axial Displacements

In Report P-61-17, the axial displacement relation, Eq. 10, was obtained by integration of the axial strain ϵ_η.

$$u_\eta = -\frac{1+\nu}{\rho}\left[\int_0^\eta \frac{\partial\psi}{\partial\rho}\,d\eta + \nu\int_0^\eta \frac{\partial\phi}{\partial\rho}\,d\eta\right] + \eta\delta + \frac{\eta^2 Z}{2} + f(\rho) \tag{10}$$

It was necessary to obtain the function $f(\rho)$ by an integration of shear strain relations when the axial displacement was not known in some radial plane.

An alternative method of obtaining axial deflections from the integration of the shear strain relation has proven more useful than Eq. 10. Elimination of $\gamma_{\rho\eta}$ from the shear strain relation

$$\gamma_{\rho\eta} = \frac{\partial u_\eta}{\partial\rho} + \frac{\partial u_\rho}{\partial\eta} = \frac{2[1+\nu]}{\rho}\frac{\partial\psi}{\partial\eta} \tag{45}$$

and the radial displacement relation

$$u_\rho = \frac{[1+\nu]}{\rho}\left\{\psi + [1-\nu]\phi\right\} + \rho\delta - \nu\rho\eta Z \quad , \tag{9}$$

results in

$$\frac{\partial u_\eta}{\partial \rho} = \frac{[1+\nu]}{\rho} \left\{ \frac{\partial \psi}{\partial \eta} - [1-\nu] \frac{\partial \phi}{\partial \eta} \right\} + \nu \rho Z \qquad (46)$$

which, upon integrating subject to the condition $u_\eta = 0$ at $\rho = 1$, produces

$$u_\eta = - \frac{\nu Z}{2} [1-\rho^2] - [1+\nu] \int_\rho^1 \left\{ \frac{1}{\rho} \frac{\partial \psi}{\partial \eta} - \frac{[1-\nu]}{\rho} \frac{\partial \phi}{\partial \eta} \right\} d\rho \quad . \qquad (47)$$

4. Results of Calculations for Axial Acceleration Loading

4.1 Two Ends Free

Calculations were made to obtain stresses and displacements in a grain having both ends free (free-free cylinder) subjected to axial acceleration loading (see Fig. 1). Results could be presented in dimensionless form with only three independent parameters - the radius ratio $\alpha = \frac{a}{b}$, the length-to-diameter ratio $\lambda = \frac{\ell}{2b}$, and Poisson's ratio ν. The displacements are represented in dimensionless form as

$$\frac{u_r E}{b^2 \gamma g} \quad \text{and} \quad \frac{u_z E}{b^2 \gamma g} \quad ,$$

where u_r and u_z are the actual radial and axial displacements respectively, E is the elastic modulus of the propellant, γ is the propellant density, and g is the axial acceleration. On most of the figures the points actually calculated are marked by appropriate symbols so that the interpolation and extrapolation of the curves would be evident. On some figures, symbols were omitted for clarity.

The dimensionless deflections A, B, and C defined in Fig. 1 are plotted in Figs. 2 through 7 as functions of α and λ for Poisson's ratio $\nu = 0.5$. The midsection displacement A approaches the displacement of an infinite cylinder for large length-to-diameter ratios as shown in Fig. 2. Note in Fig. 7 that the deflection C is not

results in

$$\frac{\partial u_\eta}{\partial \rho} = \frac{[1+\nu]}{\rho} \left\{ \frac{\partial \psi}{\partial \eta} - [1-\nu] \frac{\partial \phi}{\partial \eta} \right\} + \nu \rho Z \tag{46}$$

which, upon integrating subject to the condition $u_\eta = 0$ at $\rho = 1$, produces

$$u_\eta = -\frac{\nu Z}{2} [1-\rho^2] - [1+\nu] \int_\rho^1 \left\{ \frac{1}{\rho} \frac{\partial \psi}{\partial \eta} - \frac{[1-\nu]}{\rho} \frac{\partial \phi}{\partial \eta} \right\} d\rho \quad . \tag{47}$$

4. Results of Calculations for Axial Acceleration Loading

4.1 Two Ends Free

Calculations were made to obtain stresses and displacements in a grain having both ends free (free-free cylinder) subjected to axial acceleration loading (see Fig. 1). Results could be presented in dimensionless form with only three independent parameters - the radius ratio $\alpha = \frac{a}{b}$, the length-to-diameter ratio $\lambda = \frac{\ell}{2b}$, and Poisson's ratio ν. The displacements are represented in dimensionless form as

$$\frac{u_r E}{b^2 \gamma g} \quad \text{and} \quad \frac{u_z E}{b^2 \gamma g} \quad ,$$

where u_r and u_z are the actual radial and axial displacements respectively, E is the elastic modulus of the propellant, γ is the propellant density, and g is the axial acceleration. On most of the figures the points actually calculated are marked by appropriate symbols so that the interpolation and extrapolation of the curves would be evident. On some figures, symbols were omitted for clarity.

The dimensionless deflections A, B, and C defined in Fig. 1 are plotted in Figs. 2 through 7 as functions of α and λ for Poisson's ratio $\nu = 0.5$. The midsection displacement A approaches the displacement of an infinite cylinder for large length-to-diameter ratios as shown in Fig. 2. Note in Fig. 7 that the deflection C is not

a monotonic function of α. The variation of A, B, and C with Poisson's ratio for particular values of α and λ is shown in Figs. 8, 9, and 10.

Figures 11 through 14 and Figs. 15 through 18 illustrate the effect of λ and α on the radial and shear stress respectively at the propellant motor case interface for a Poisson's ratio of $\nu = 0.5$. A singularity in the stress distribution occurs at the corner formed by a free end and the motor case. Thus, any stresses calculated near these points are physically meaningless because any real material will deviate from the assumed model. In the figures illustrating stress distribution, the stresses near this singularity are indicated by dashed lines. The effect of this singularity on the numerical solution has not been fully evaluated but is believed to be small even at small distances from the singular point. The effects of Poisson's ratio on the displacements near the end are complex, but at points removed from the ends the stresses are not highly dependent on Poisson's ratio.

4.2 One End Fixed

For cylinders having one end bonded (fixed-free cylinder), as illustrated in Fig. 19, results similar to those obtained for the free-free cylinders are presented in Figs. 20 through 43. Note that the proper interpretation of the sign of the deflection and stresses depends on the direction of acceleration while the magnitude is independent of the direction of acceleration. Figs. 20 through 25 demonstrate the variation of the quantities A, B, and C as defined in Fig. 19 for various values of λ and α but only for Poisson's ratio of 0.5. Figs. 26 through 27 demonstrate the variation of A, B, and C with Poisson's ratio. Although these figures are not a complete parameter study, they do indicate the complex nature of the dependence on Poisson's ratio.

Figs. 29 through 33 show the load carried by the end bond as the percentage of the total load carried by the motor case in accelerating the grain. Figs. 29 and 30 are crossplots in α and λ of this data for $\nu = 0.5$. Figs. 31 through 33 illustrate the dependence on Poisson's ratio.
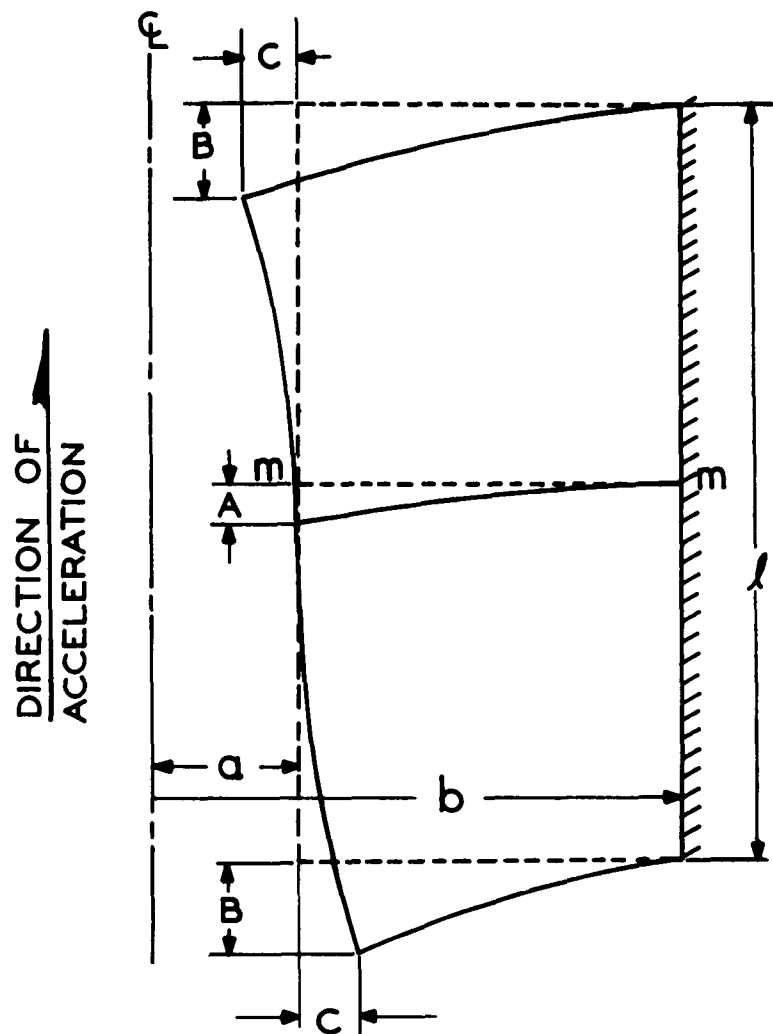
Fig. 1   Cross section of cylinder with free ends deformed by acceleration.
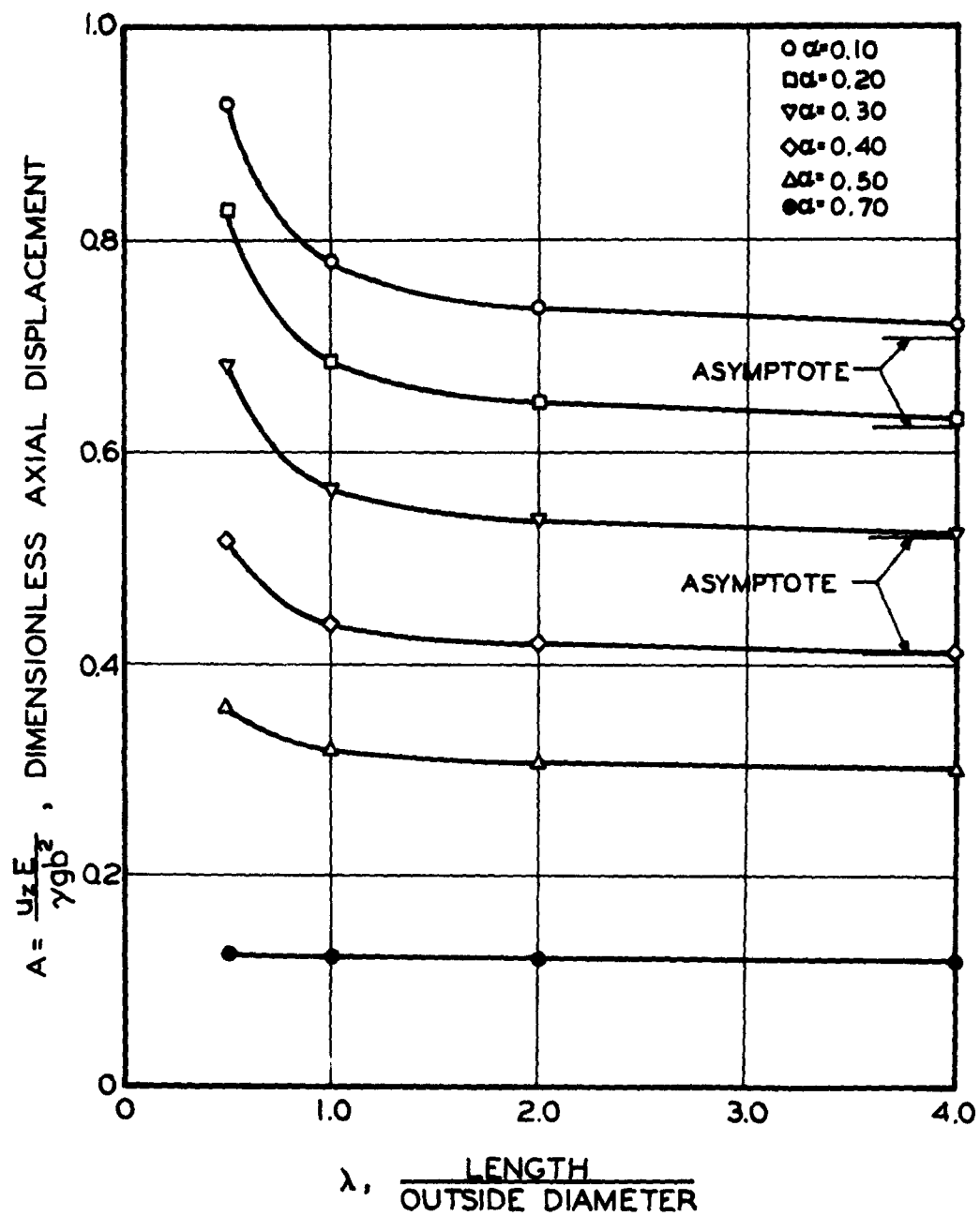
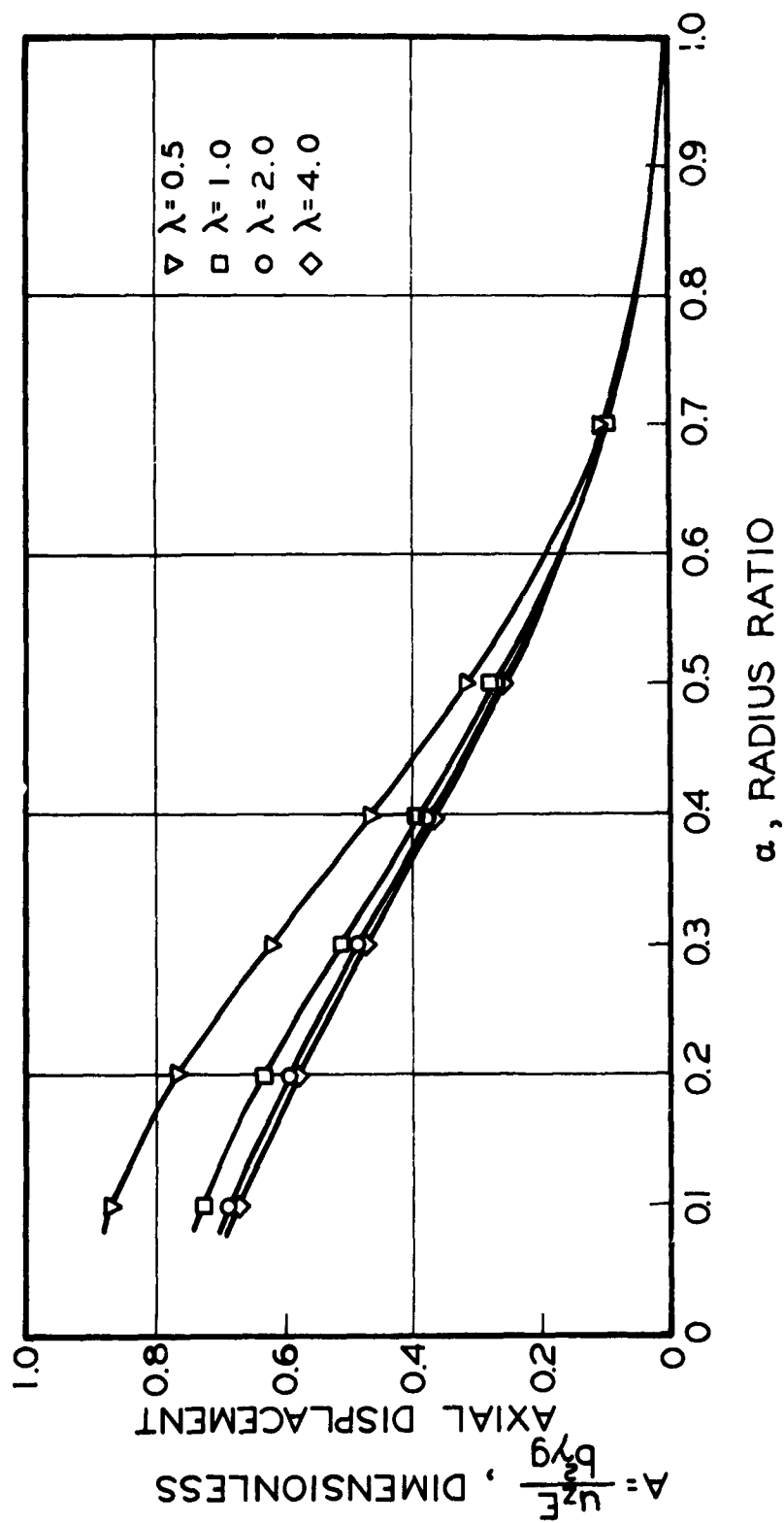Fig. 2 Axial displacement at midsection of free-free cylinder, $\nu = 0.5$.

Fig. 3 Axial displacement of free-free cylinder, $\nu = 0.5$.
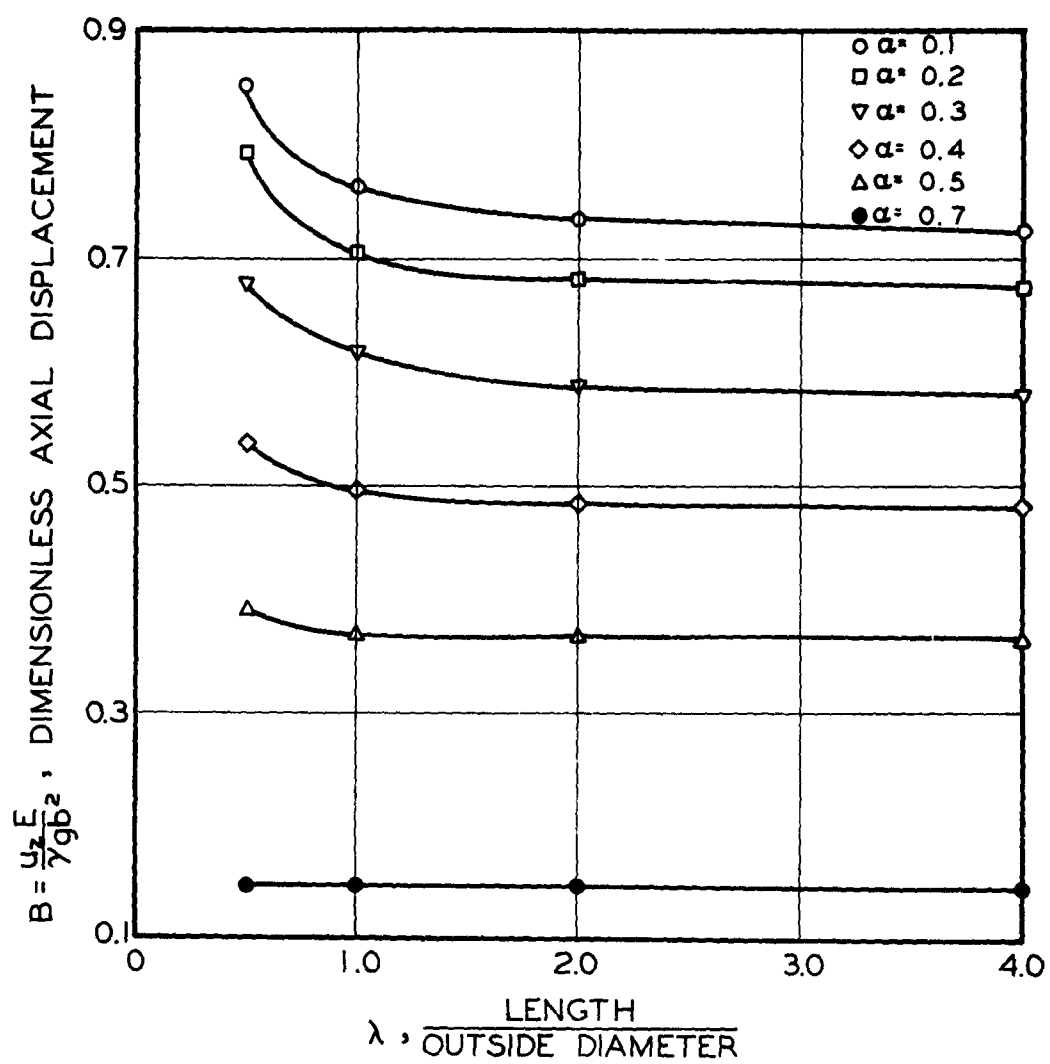
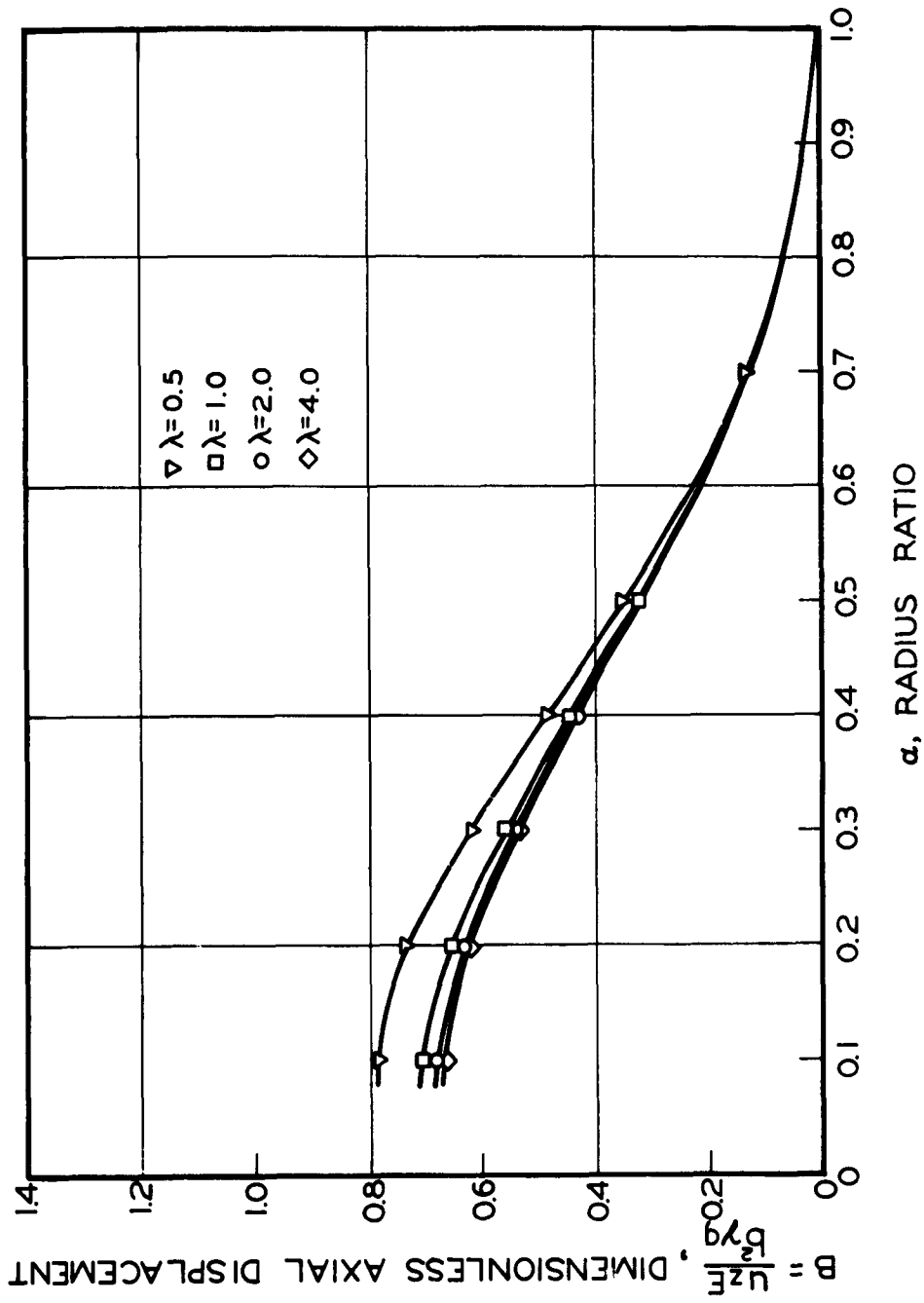Fig. 4 Axial displacement of corner of free - free cylinder , $\nu = 0.5$.

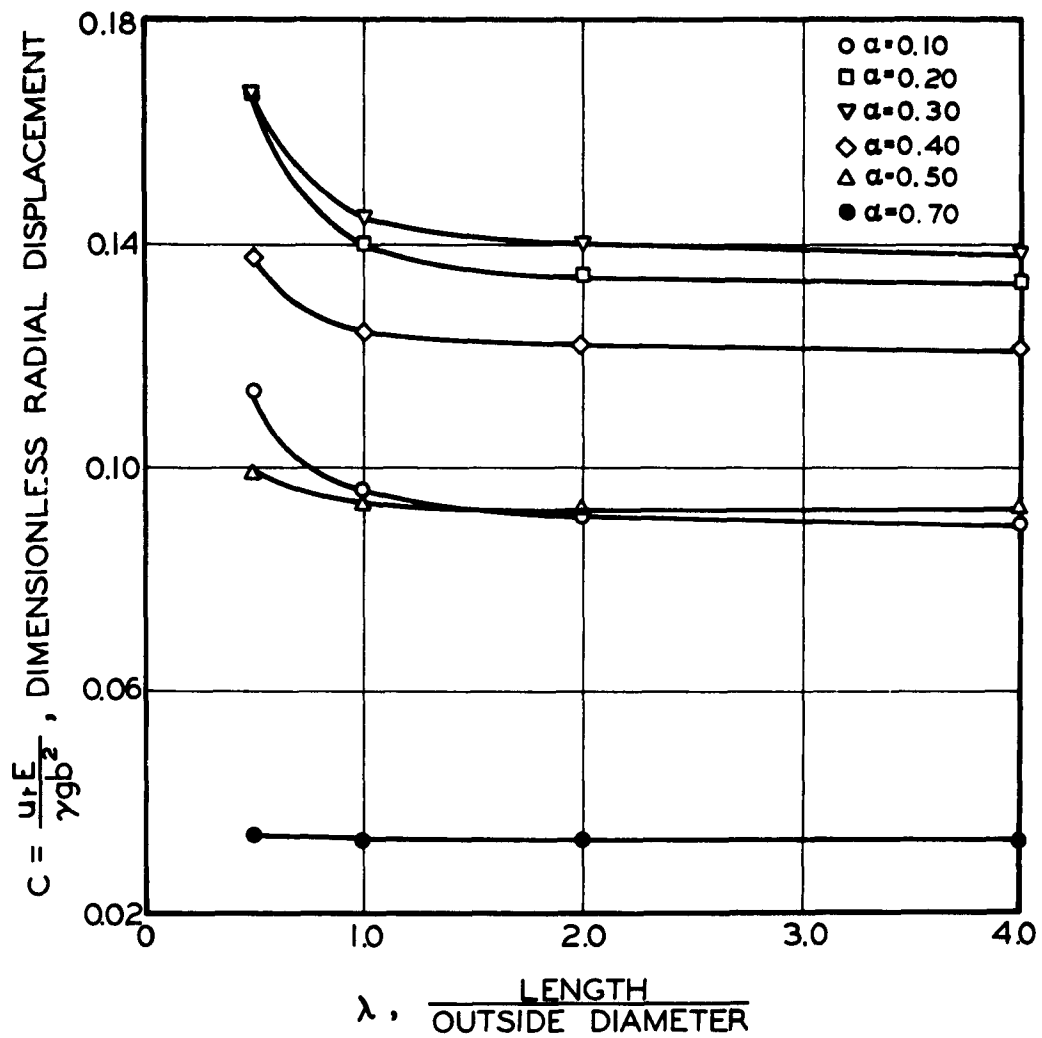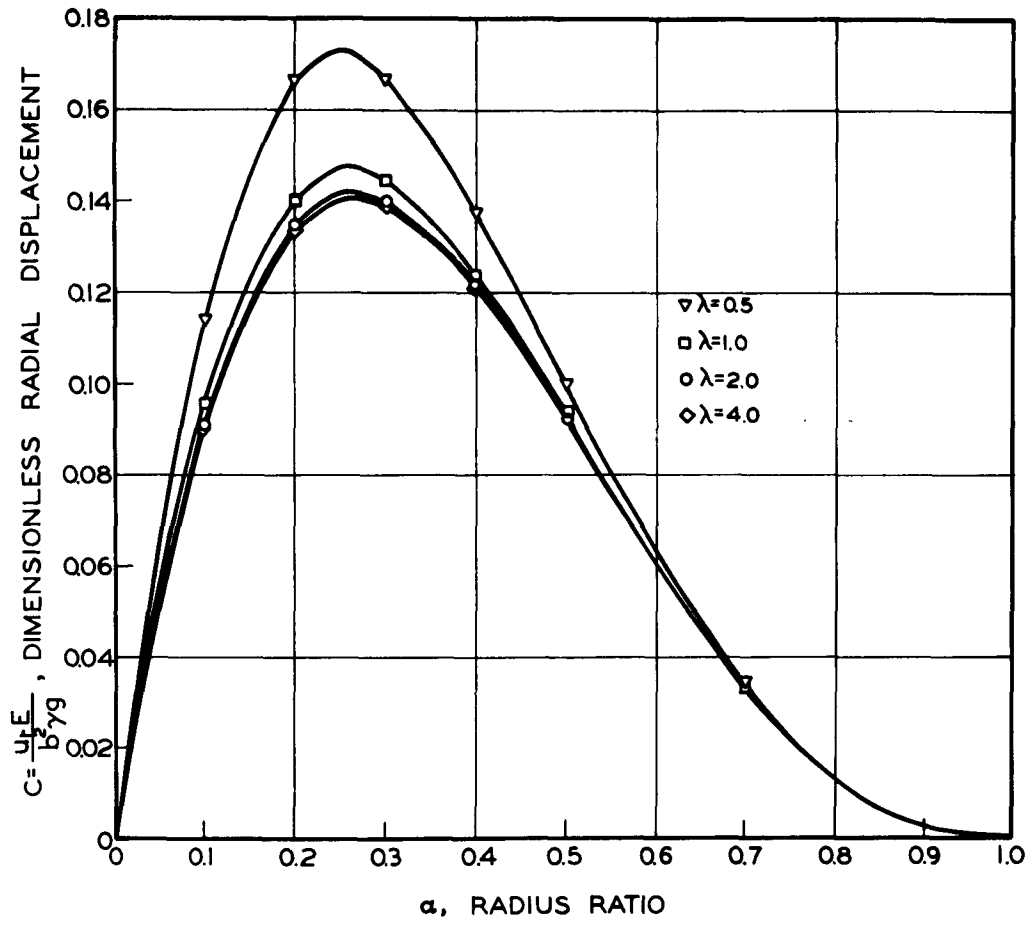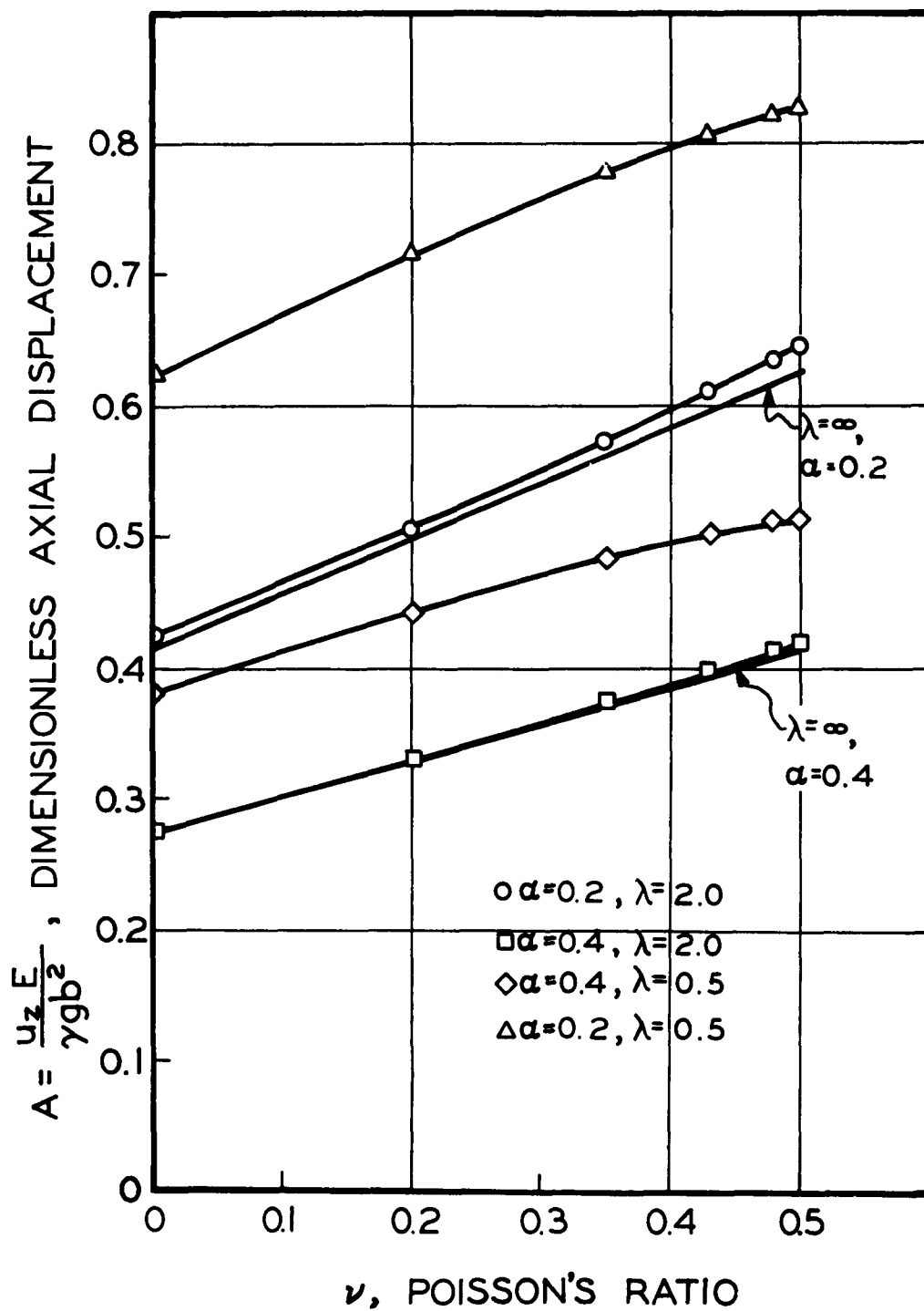Fig. 5 Axial displacement of corner of free-free cylinder, $\nu = 0.5$.
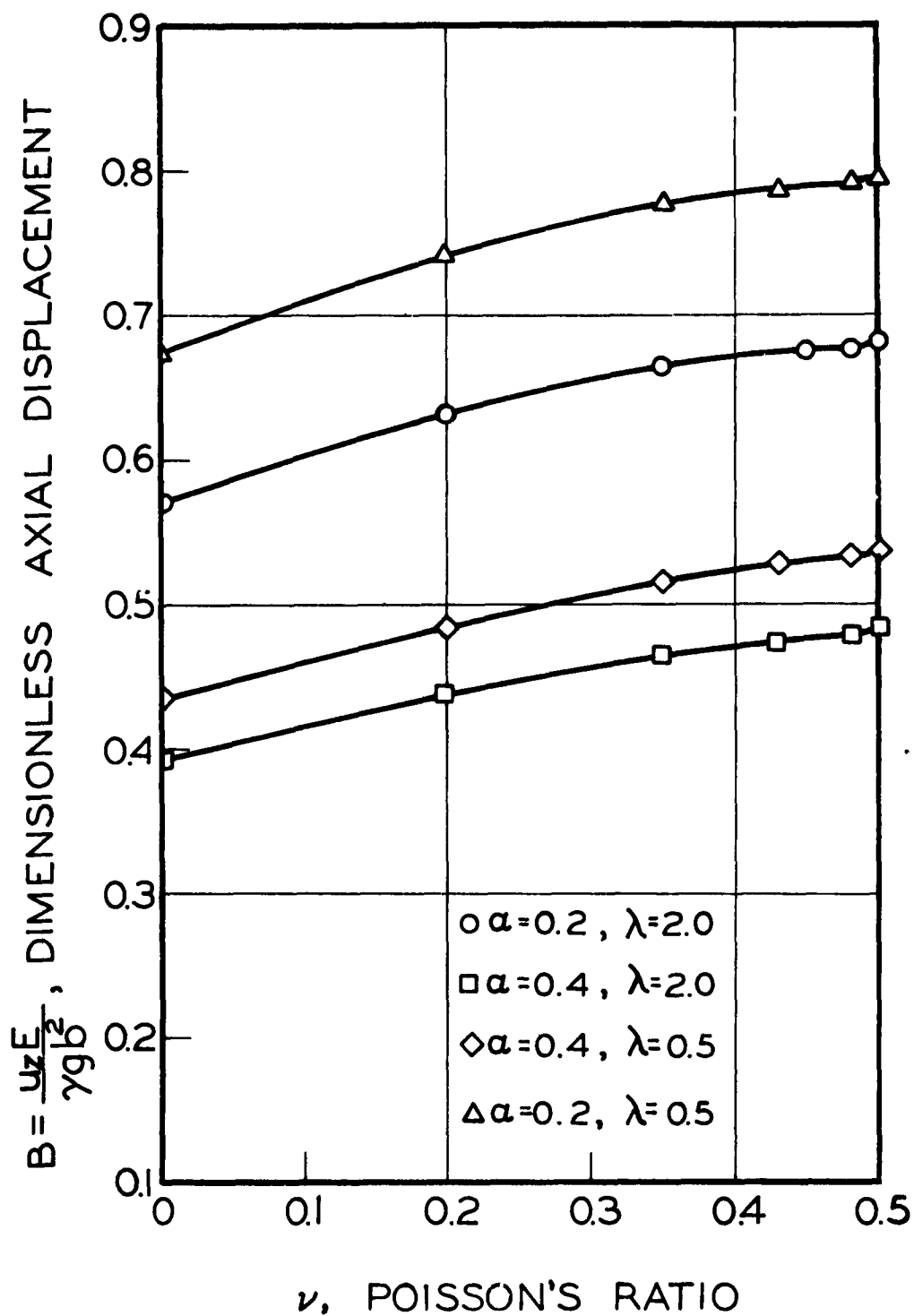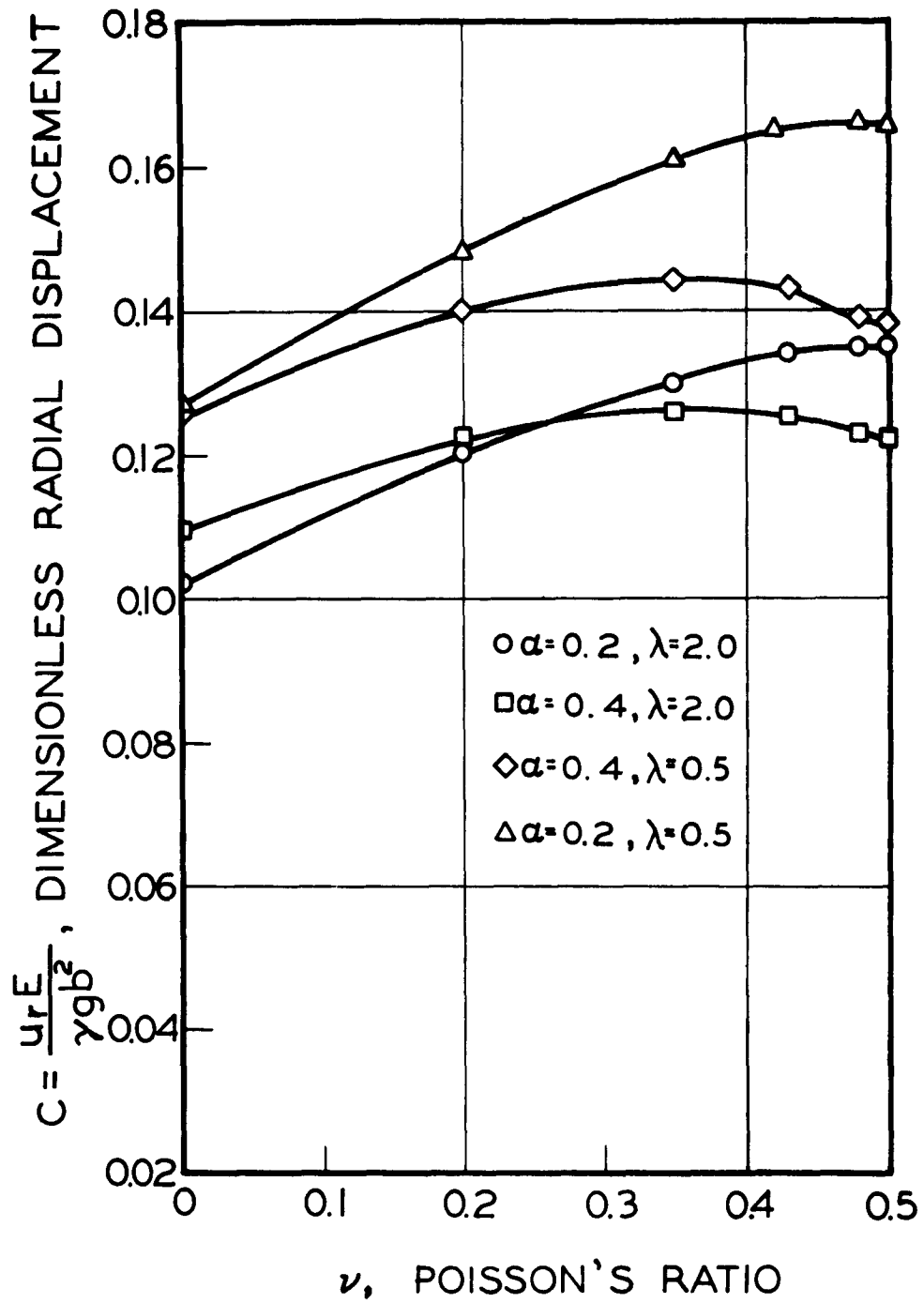
Fig. 6 Radial displacement of corner of free-free cylinder, $\nu = 0.5$.

Fig. 7 Radial displacement of corner of free-free cylinder, $\nu = 0.5$.

Fig. 8 Maximum axial displacement at midsection of free-free cylinder.

Fig. 9 Axial displacement of corner of free-free cylinder.

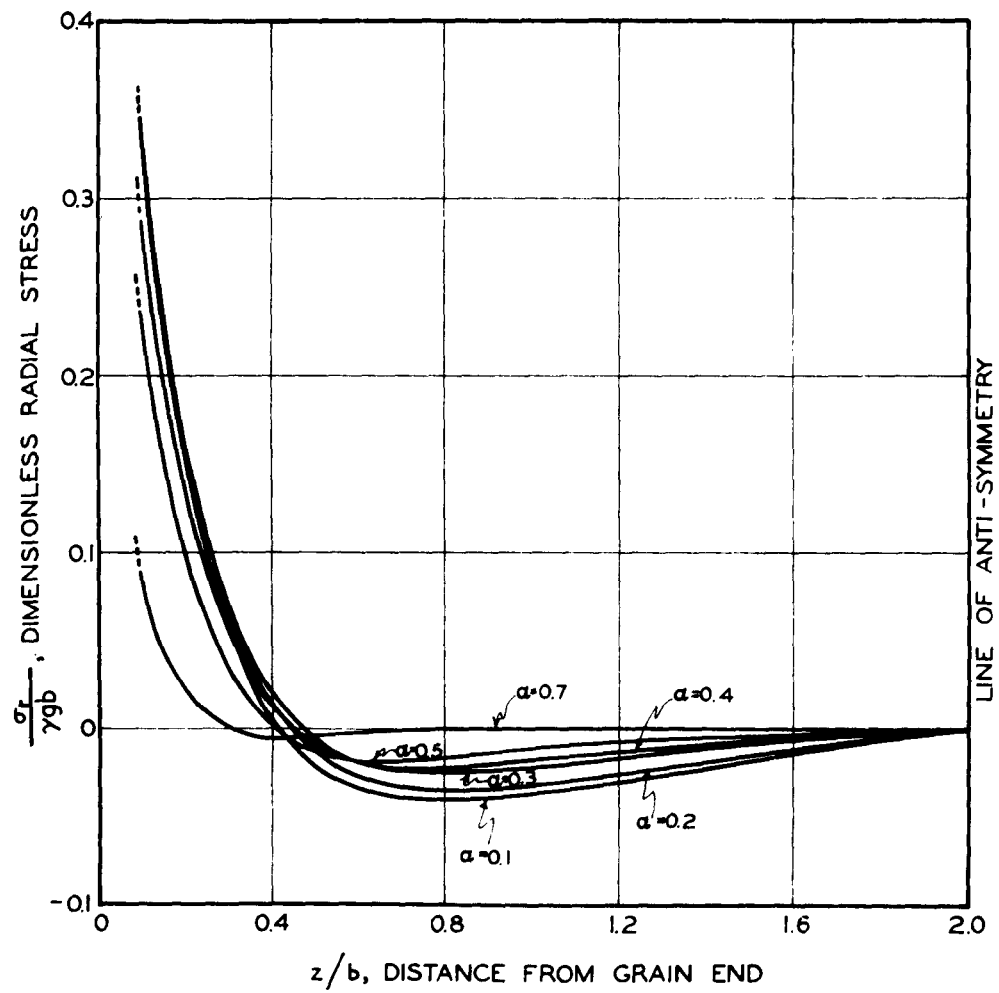Fig. 10   Radial displacement of corner of free-free cylinder.
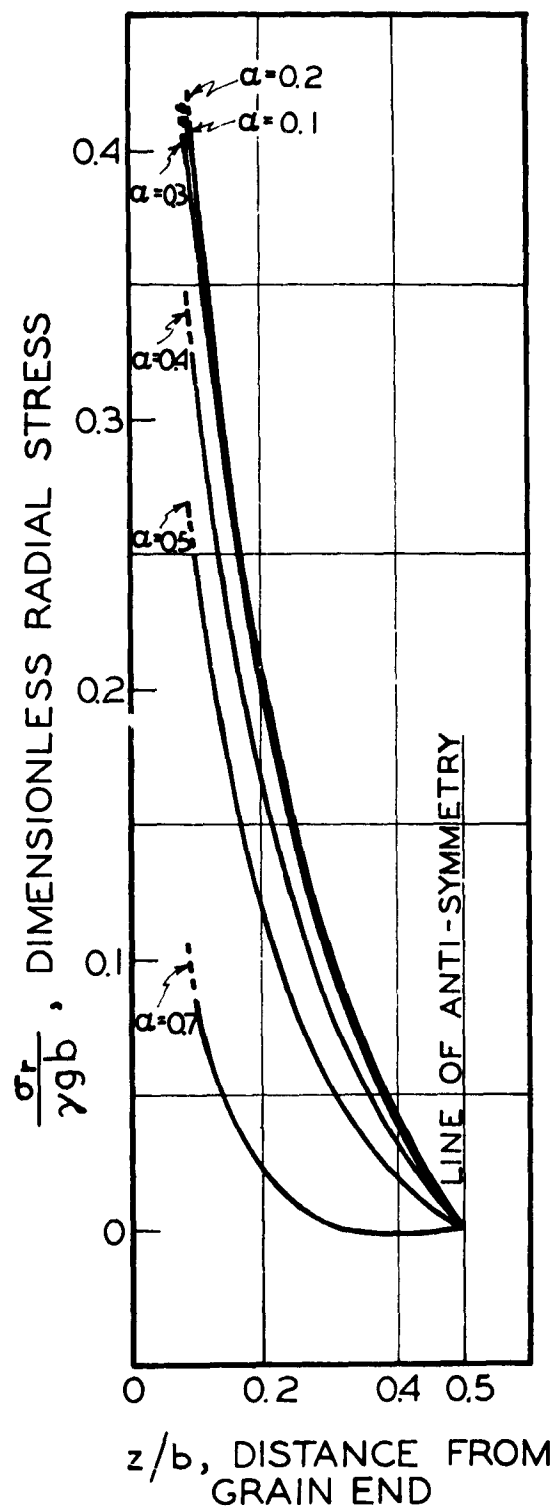
Fig. 11   Dimensionless radial stress at propellant-motor case interface, λ=0.5, ν = 0.5.
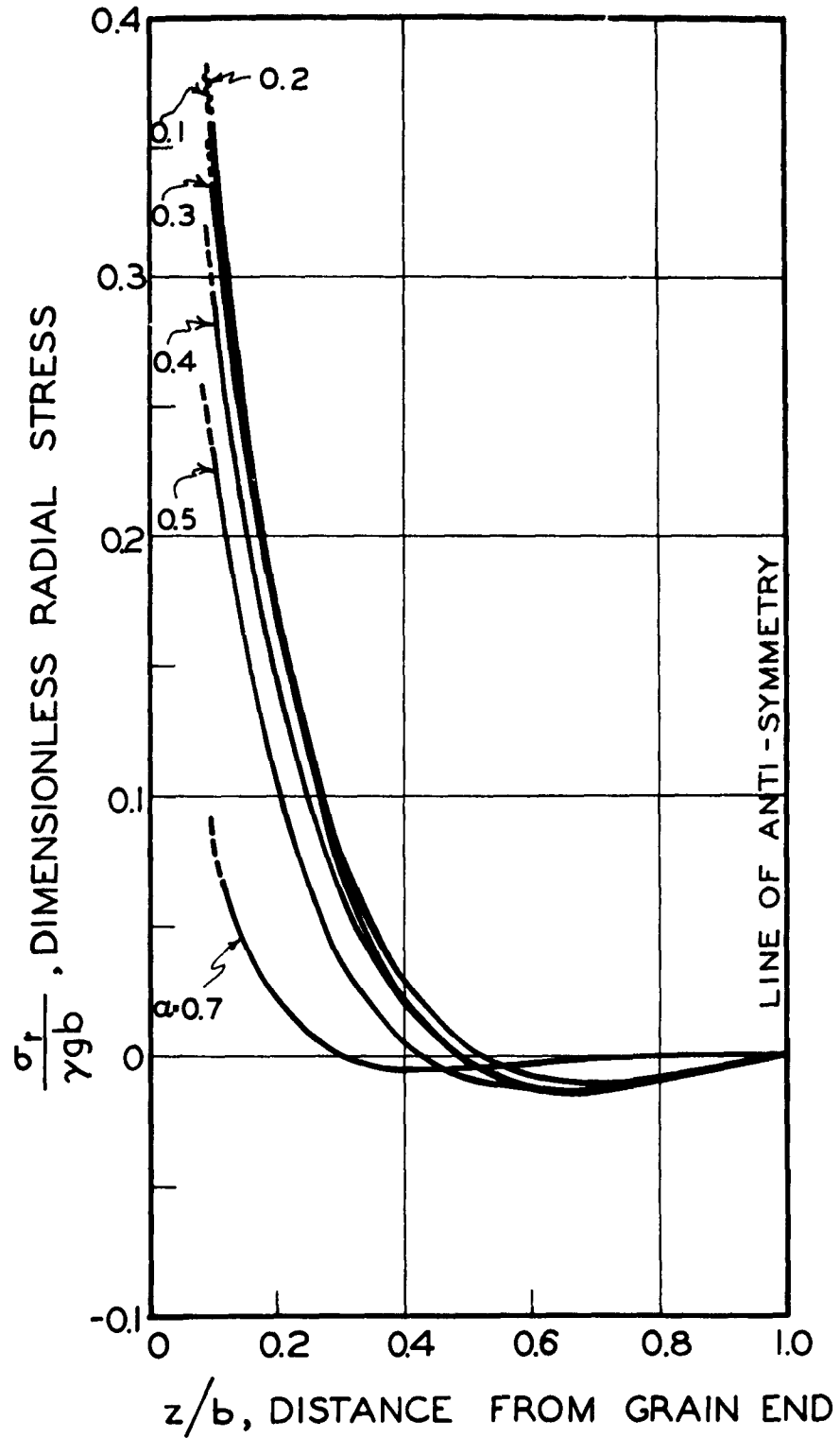
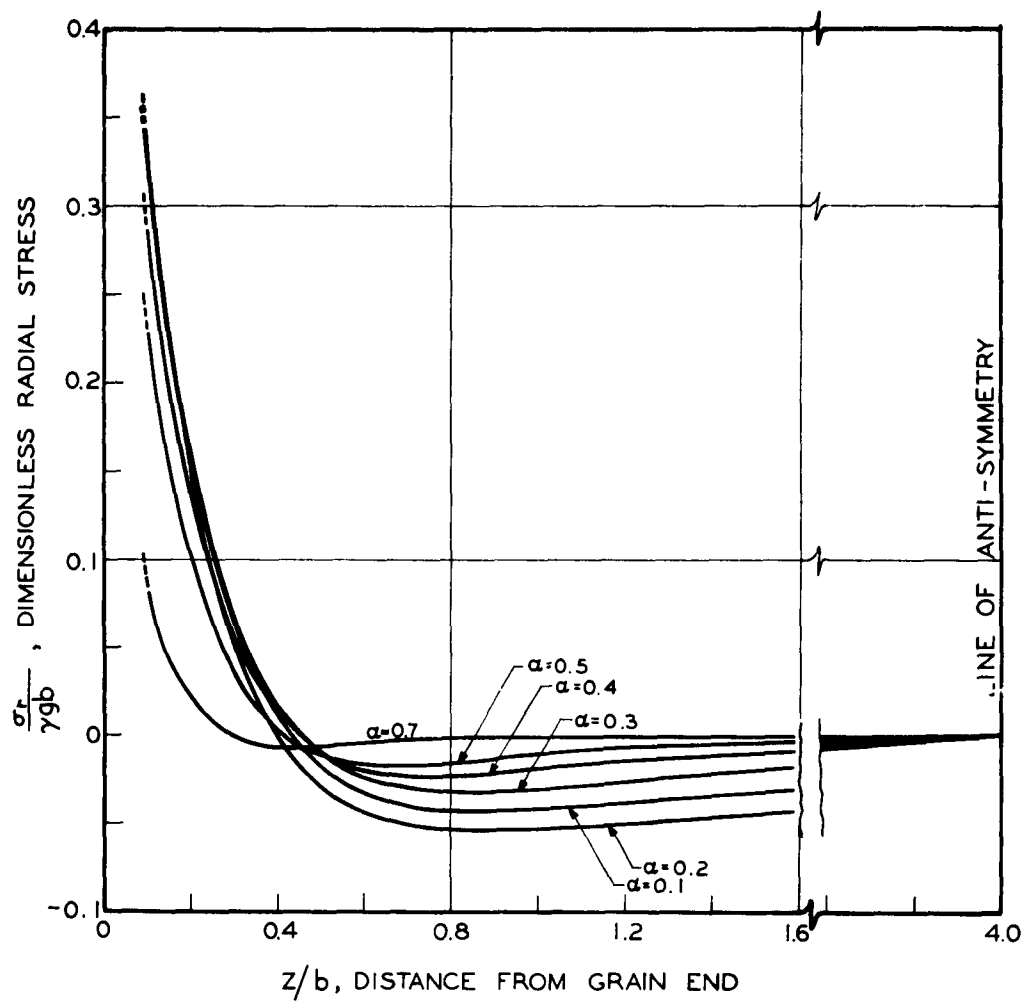Fig. 12 Dimensionless radial stress at propellant-motor case interface, λ=1.0, ν=0.5.

Fig. 13   Dimensionless radial stress at propellant-motor case interface, $\lambda=2.0$, $\nu=0.5$.

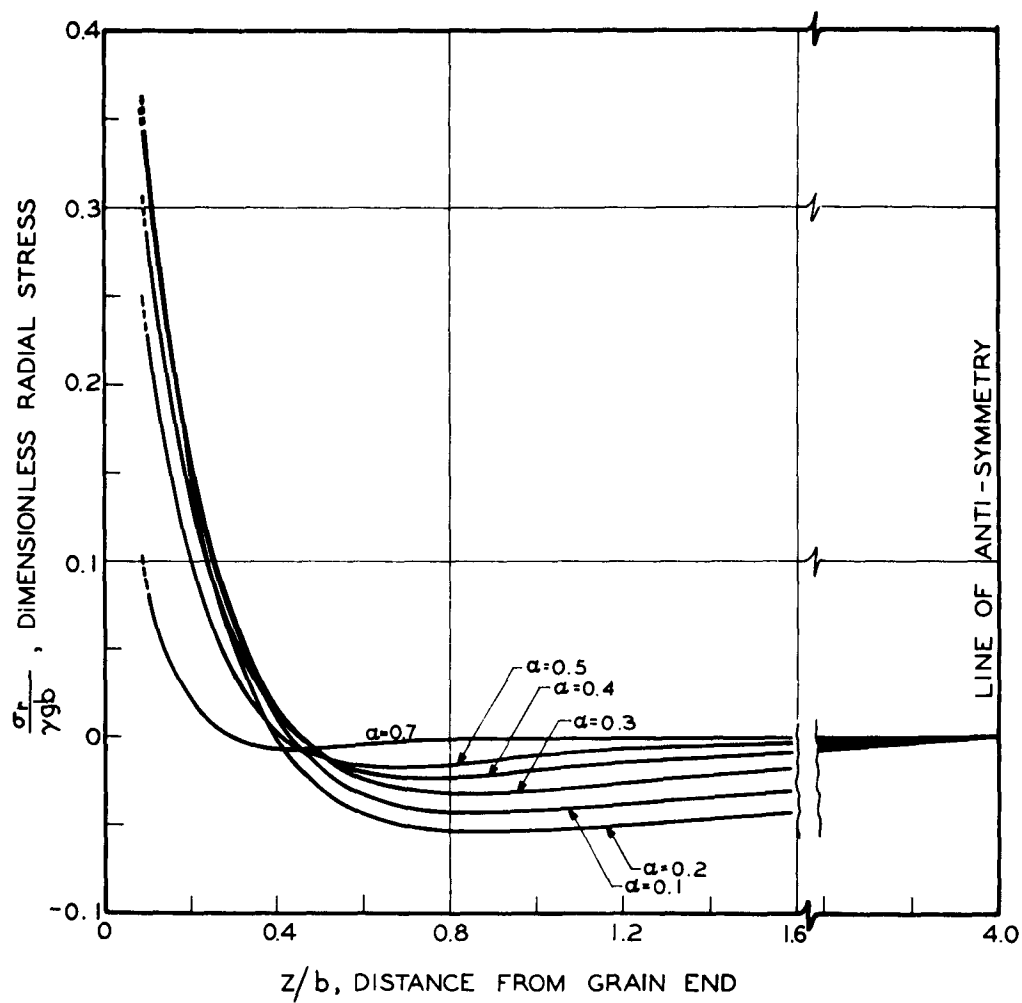Fig. 14 Dimensionless radial stress at propellant-motor case interface, $\lambda=4.0$, $\nu=0.5$.
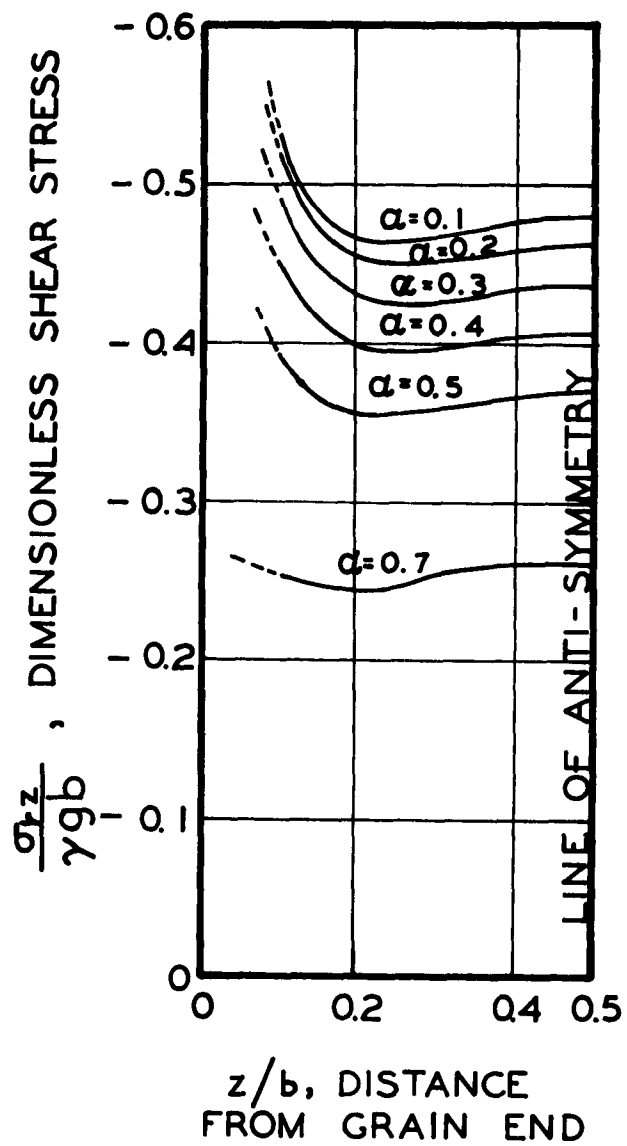
Fig. 14   Dimensionless radial stress at propellant-motor case interface, λ=4.0, ν=0.5.

Fig. 15 Dimensionless shear stress at propellant-motor case interface, λ=0.5, ν=0.5.
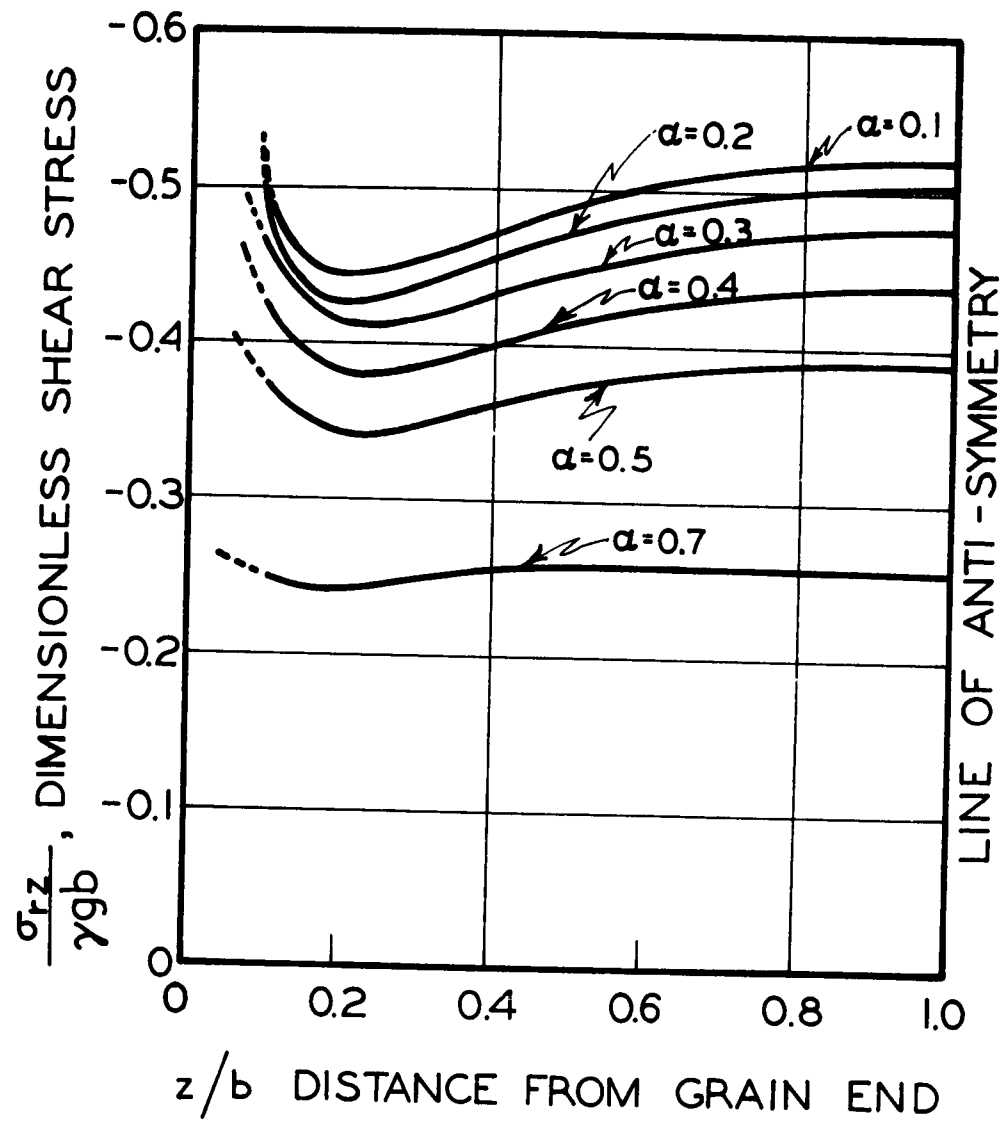
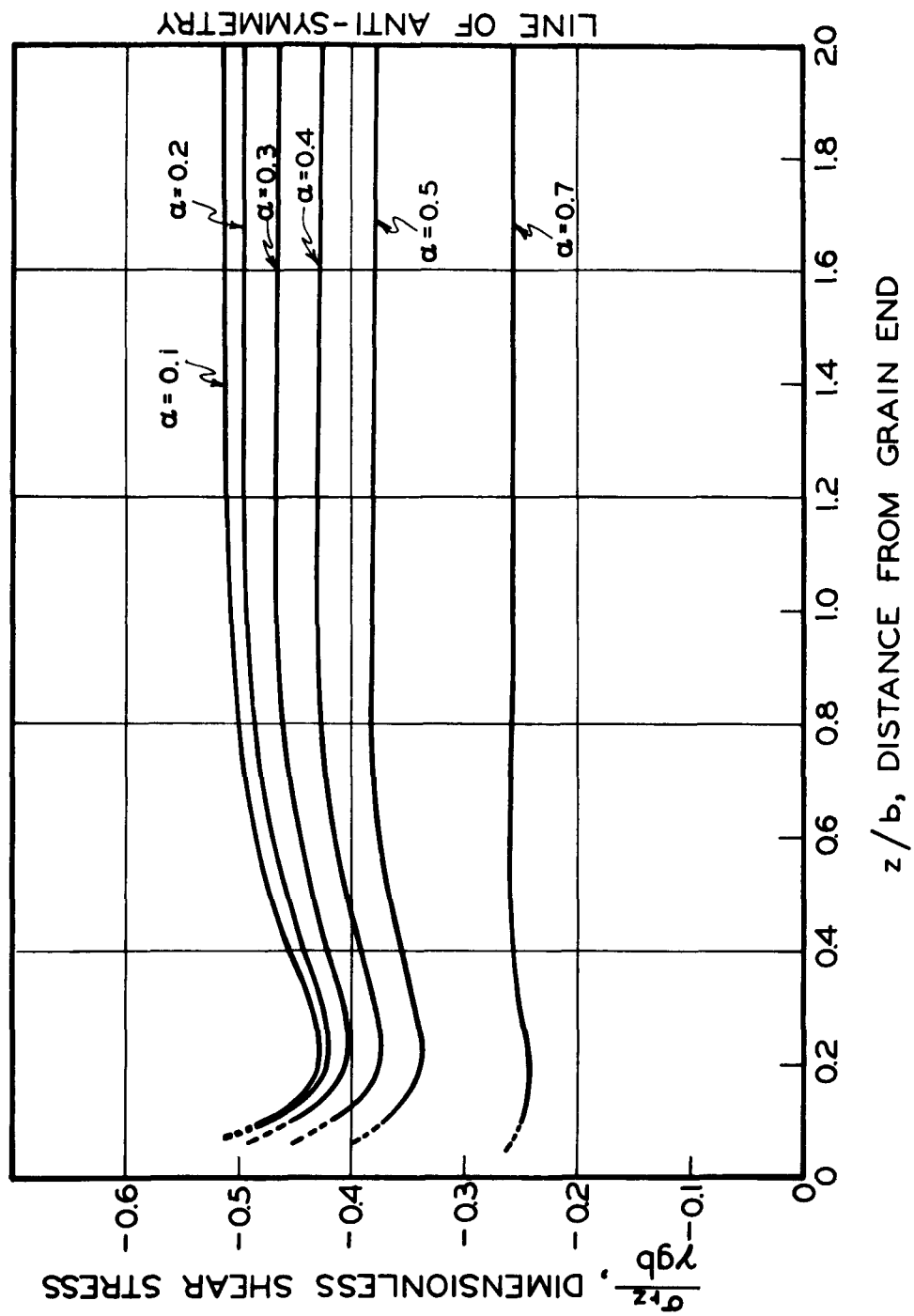Fig. 16 Dimensionless shear stress at propellant-motor case interface, $\lambda = 1.0$, $\nu = 0.5$.

Fig. 17 Dimensionless shear stress at propellant-motor case interface, $\lambda = 2.0$, $\nu = 0.5$.
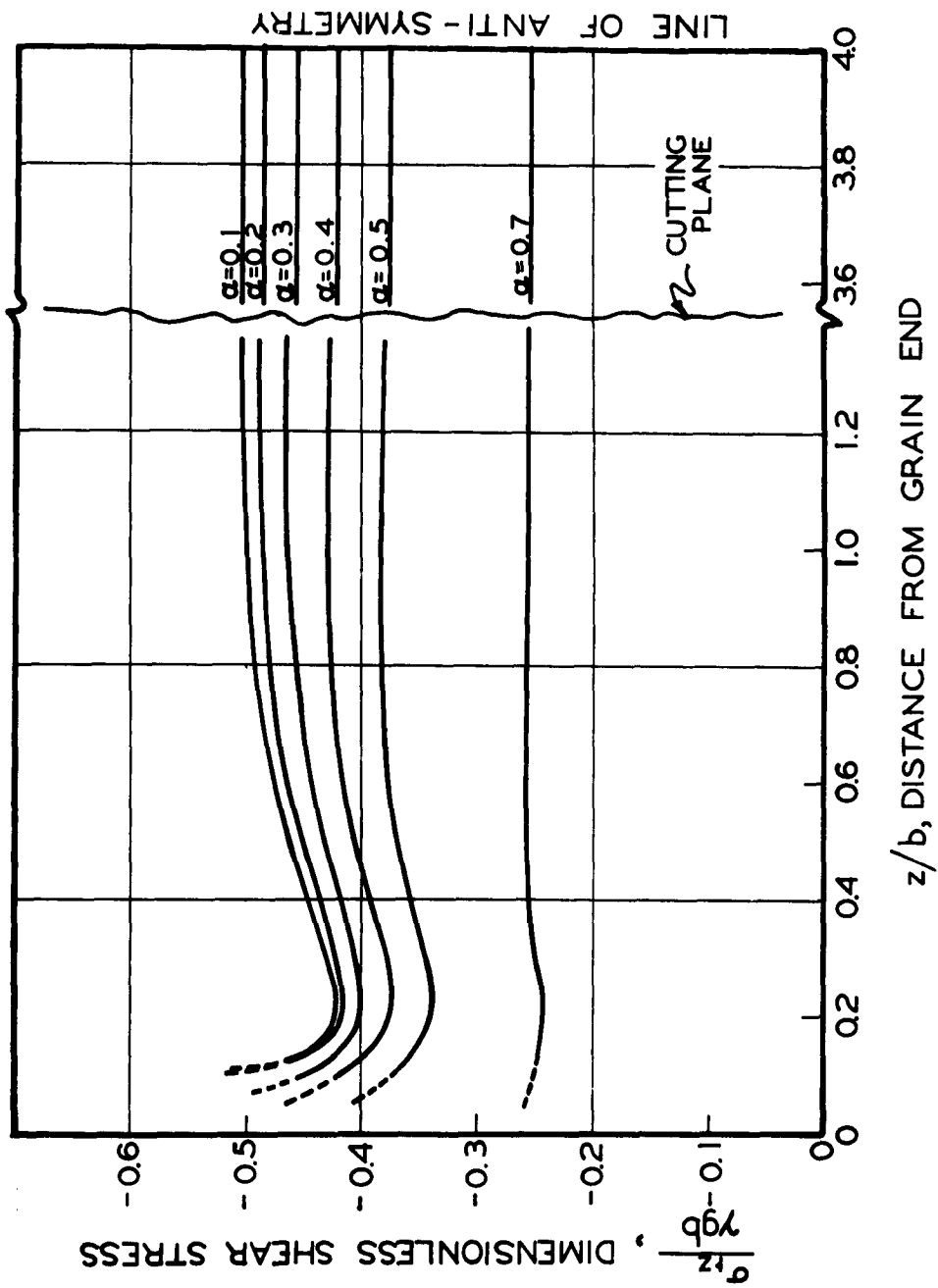
Fig. 18 Dimensionless shear stress at propellant-motor case interface, $\lambda=4.0$, $\nu=0.5$.

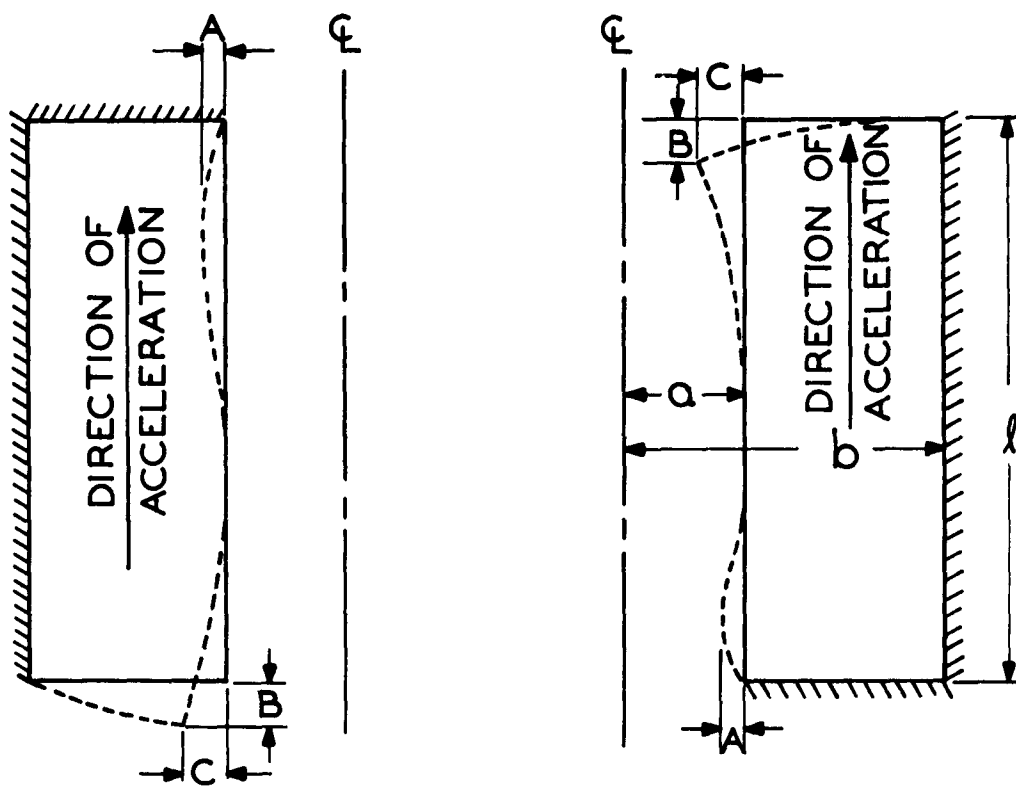Fig. 19 Cross sections of cylinders with one fixed end, deformed by acceleration.

Fig. 20 Maximum radial displacement near fixed end of fixed-free cylinder, $\nu = 0.5$.

Fig. 21 Maximum radial displacement near fixed end of fixed-free cylinder, $\nu = 0.5$.

Fig. 22 Axial displacement of free corner of fixed-free cylinder, $\nu = 0.5$.
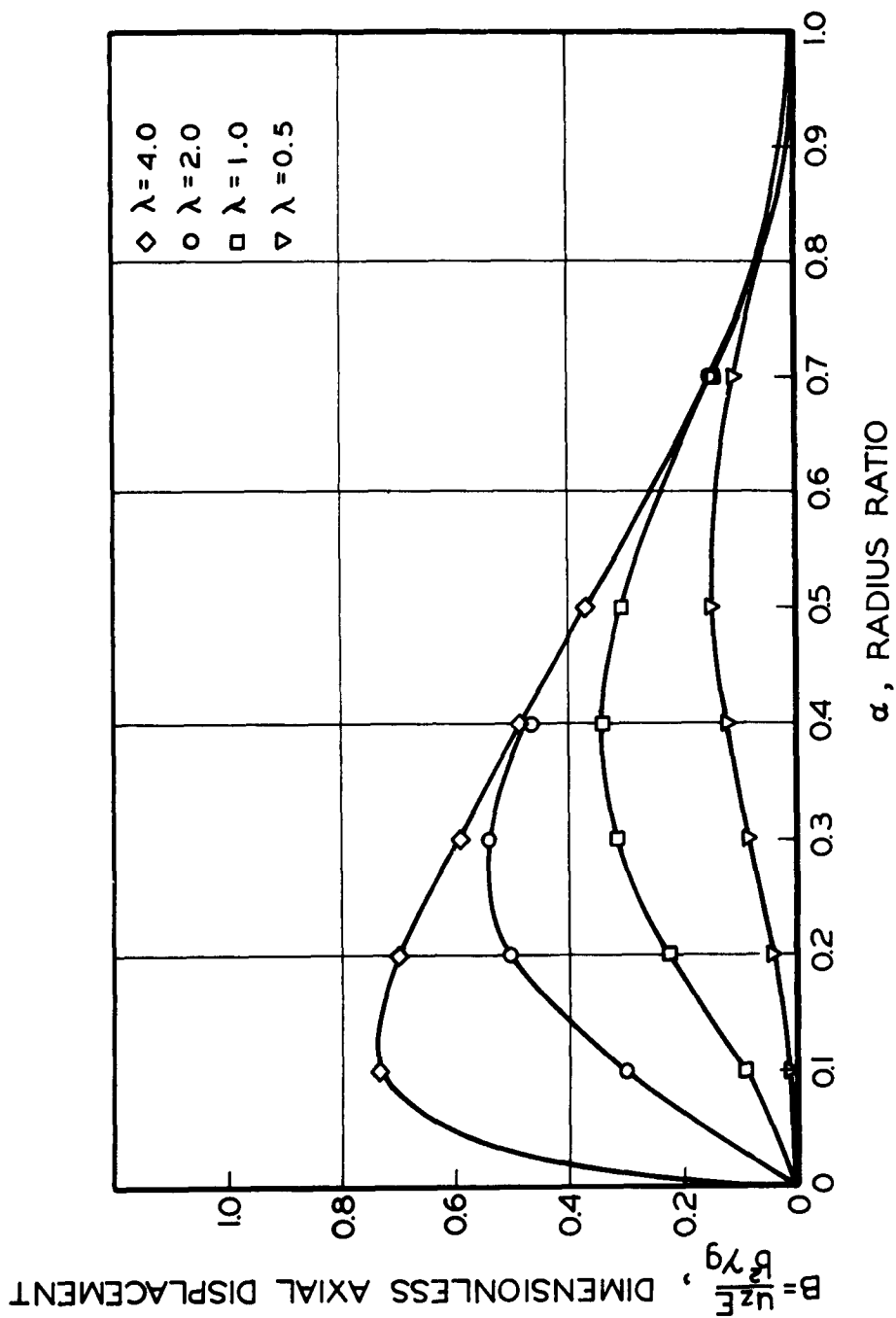
Fig. 23 Axial displacement of free corner of fixed-free cylinder, $\nu = 0.5$.
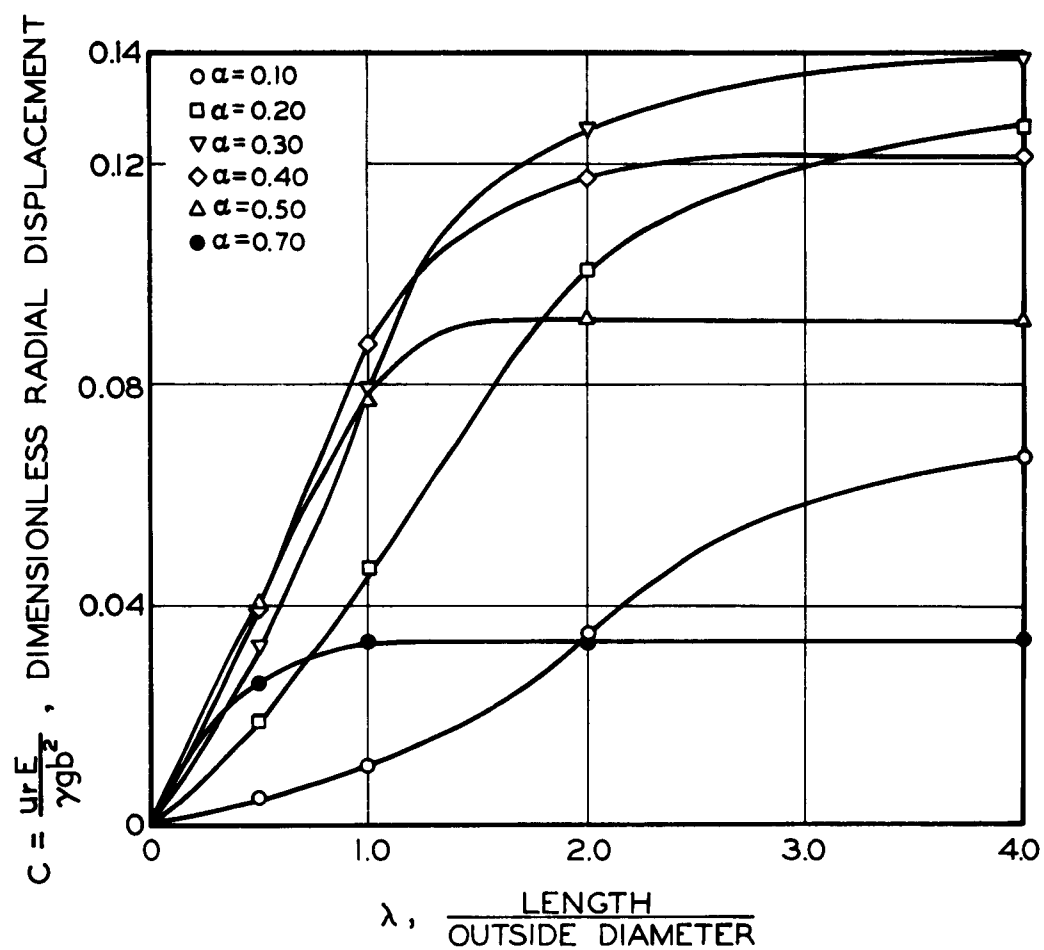
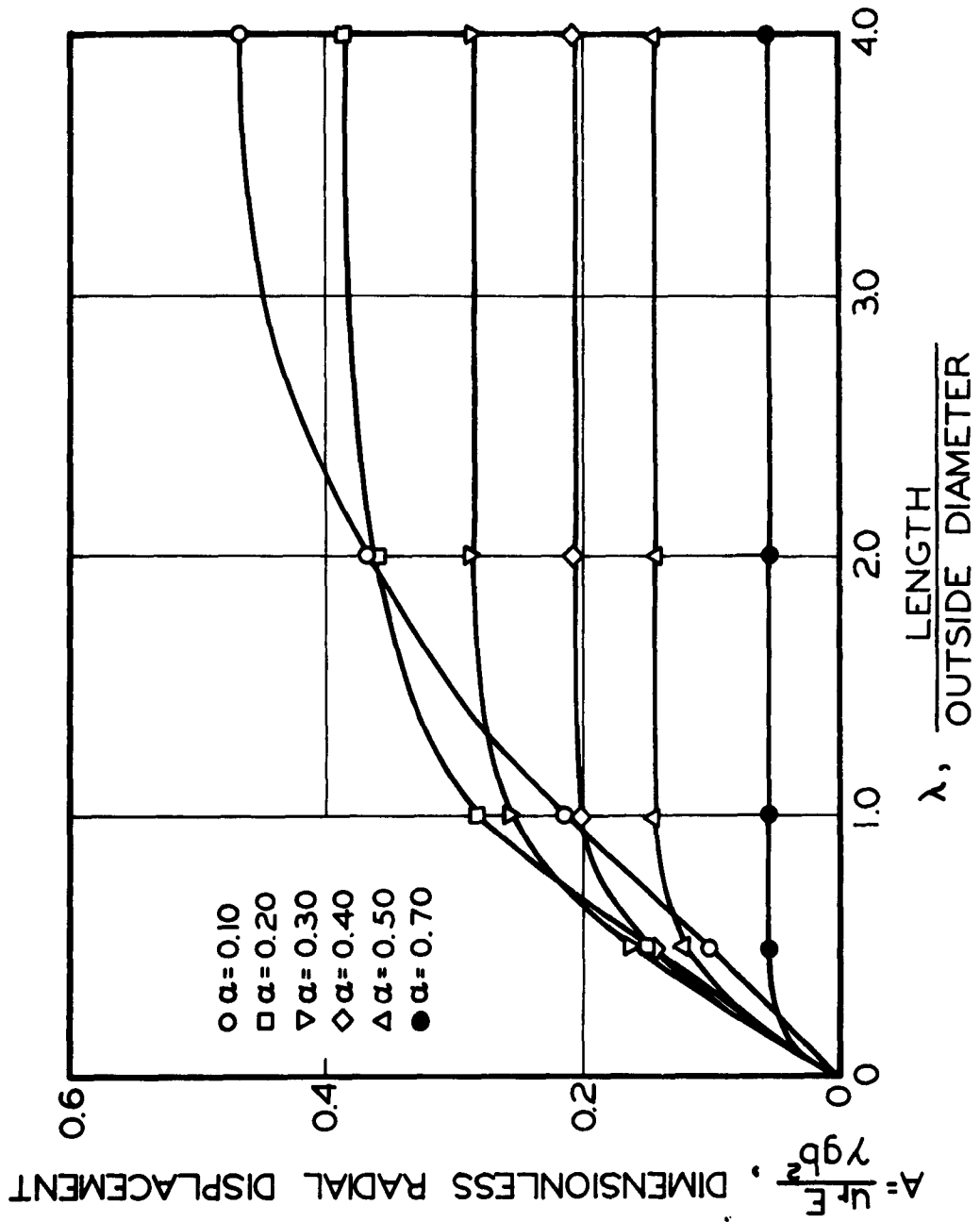Fig. 24 Radial displacement of free corner of fixed-free cylinder, $\nu = 0.5$.
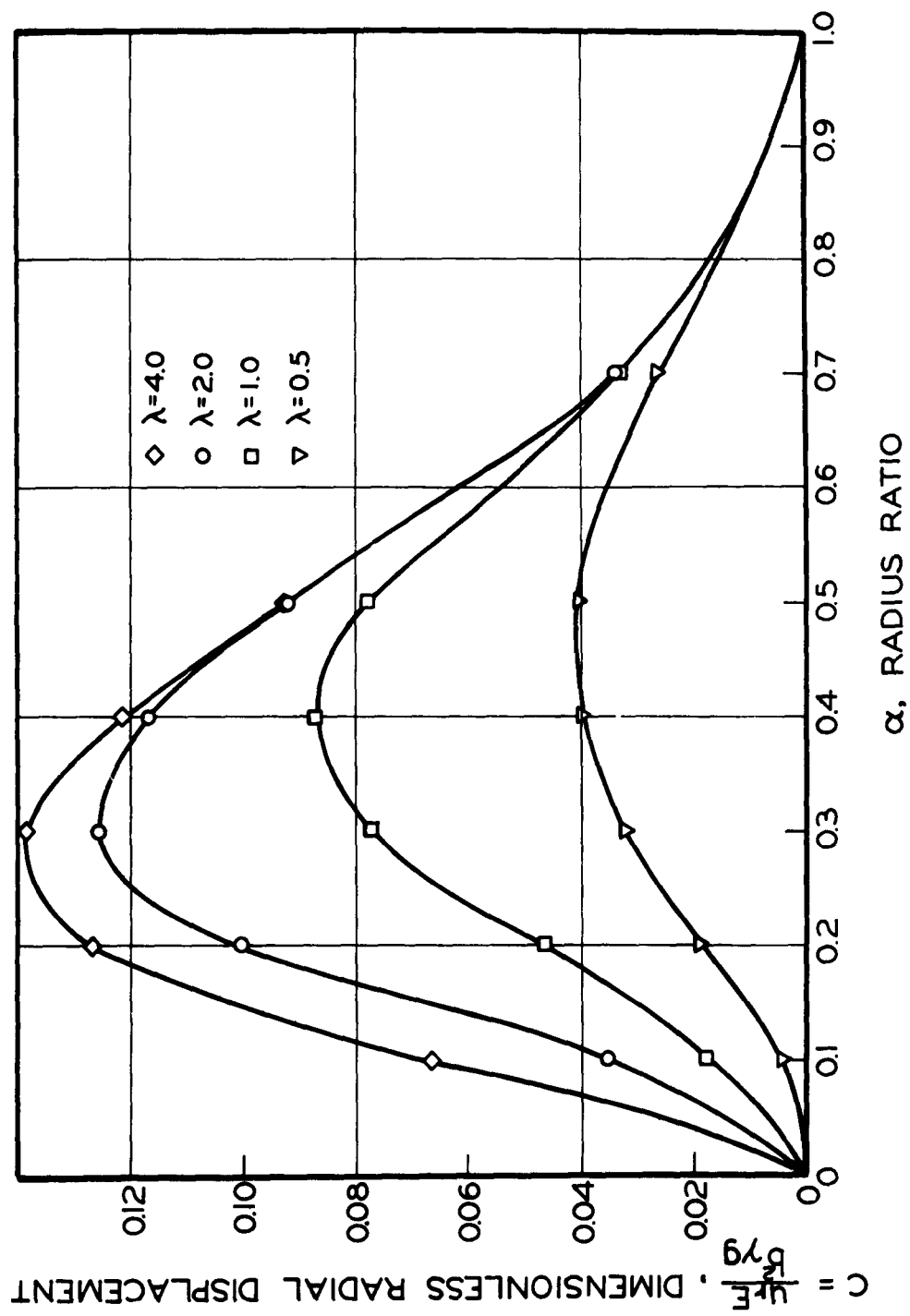
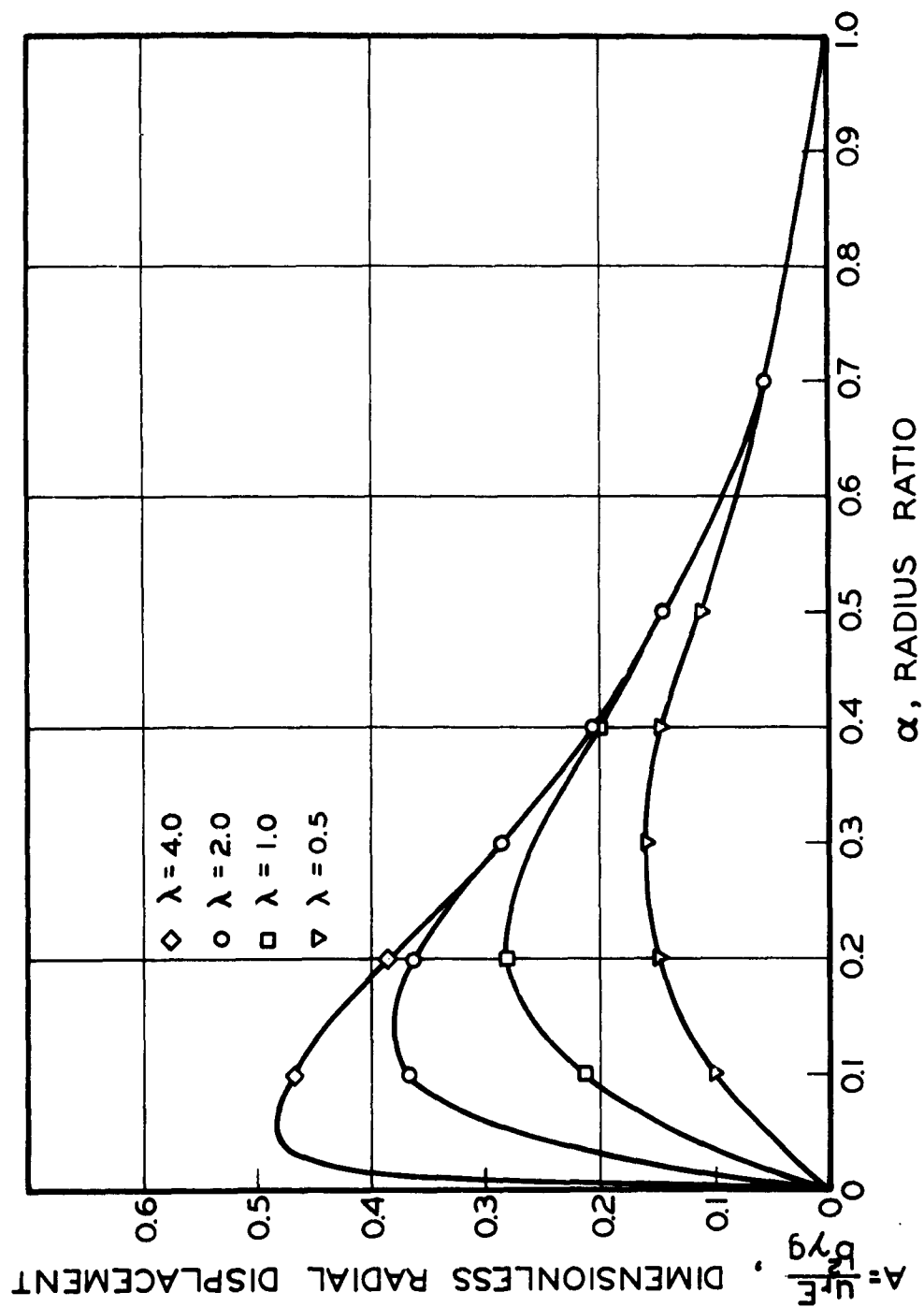Fig. 25 Radial displacement of free corner of fixed-free cylinder, $\nu = 0.5$.
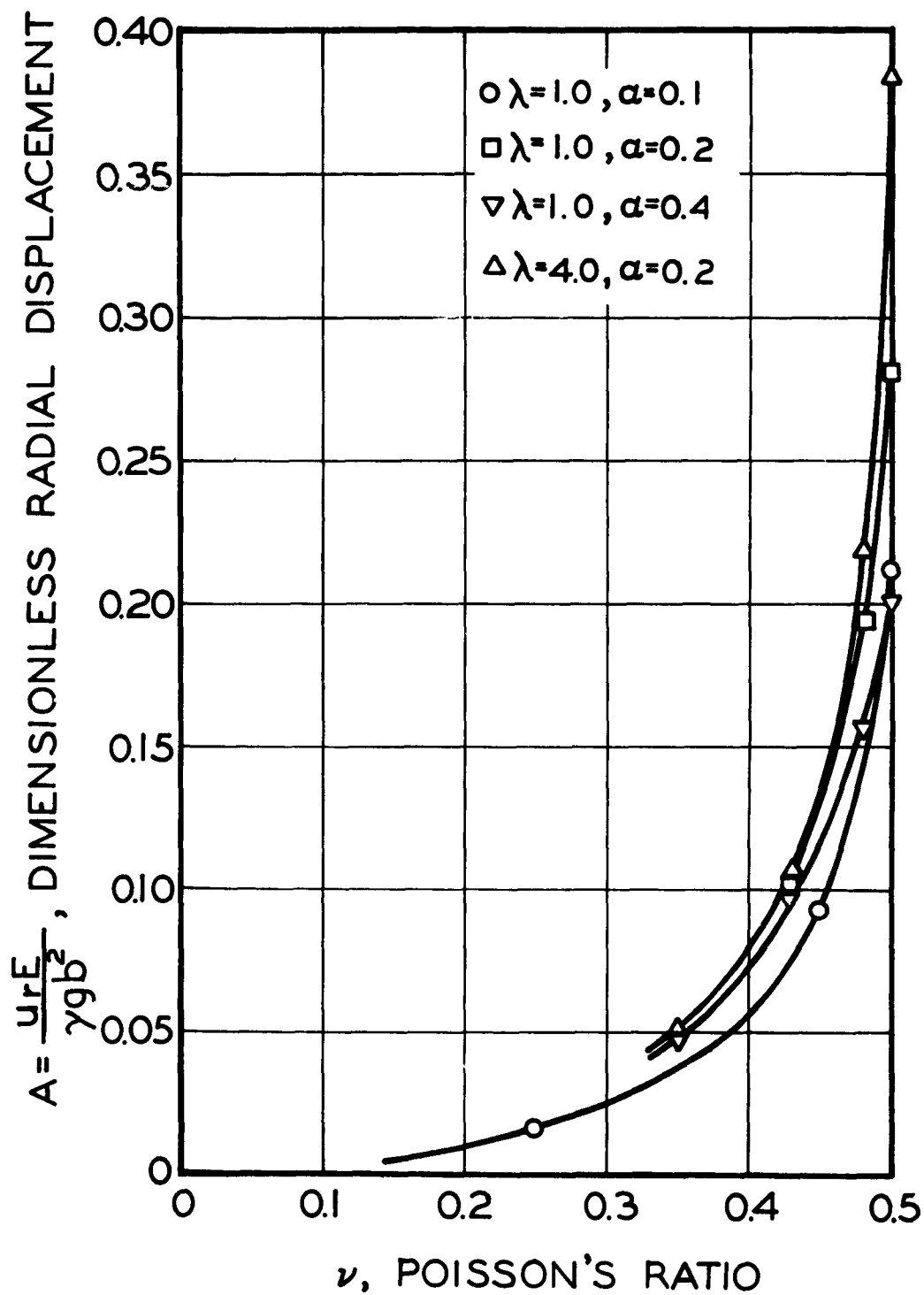
Fig. 26   Maximum radial displacement near fixed end of fixed-free cylinder.
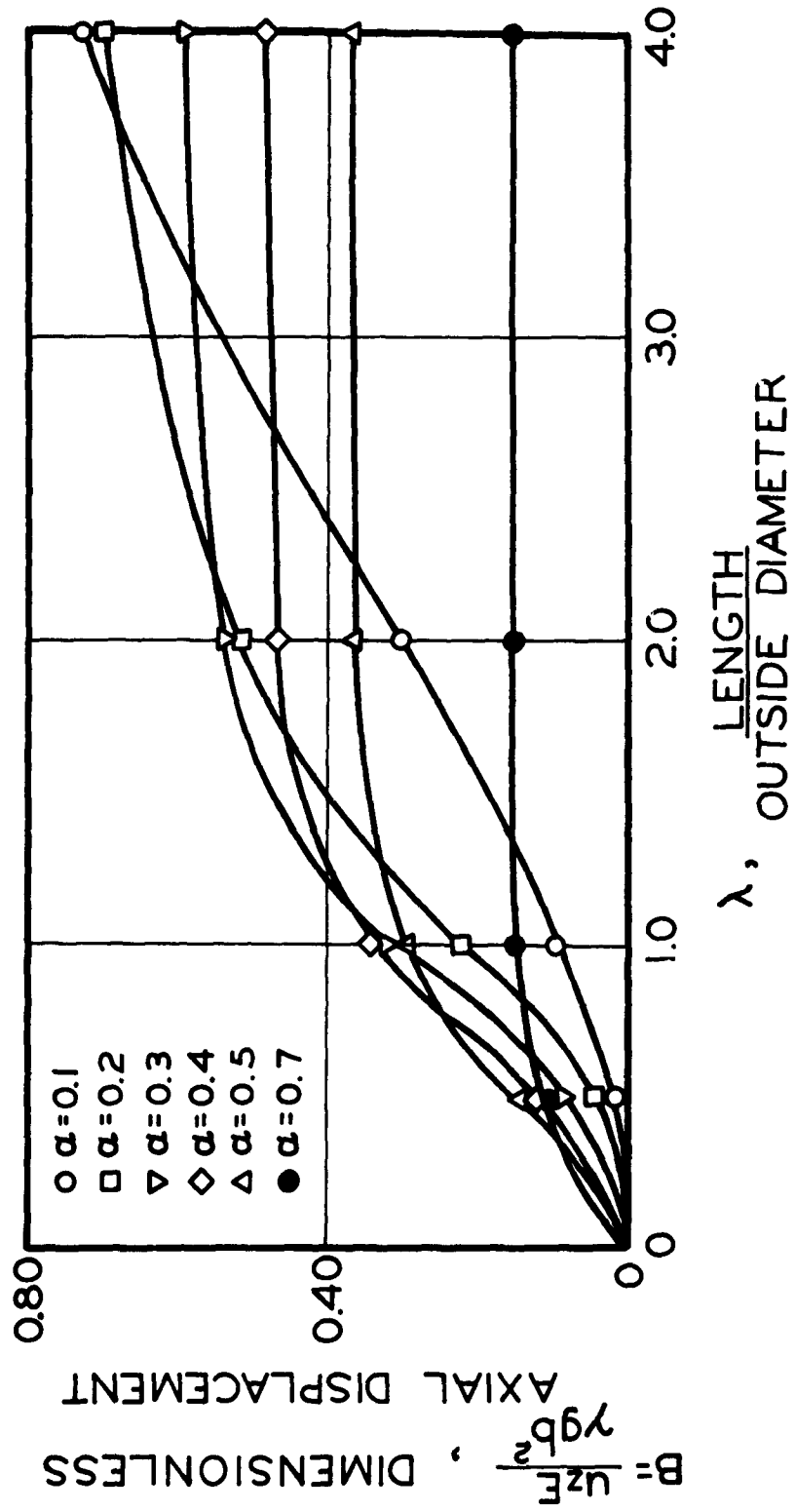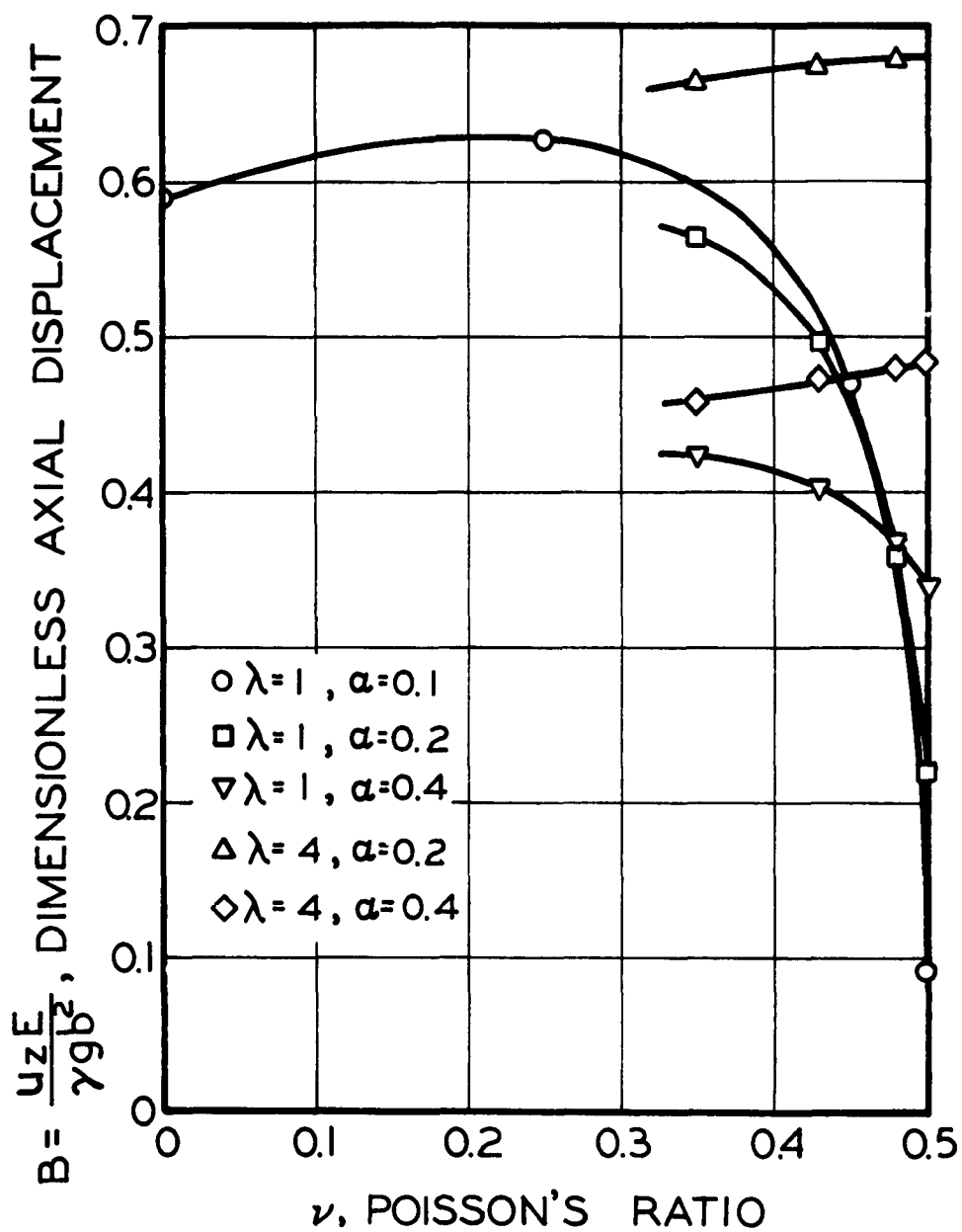
Fig. 27   Axial displacement of free corner of fixed-free cylinder.
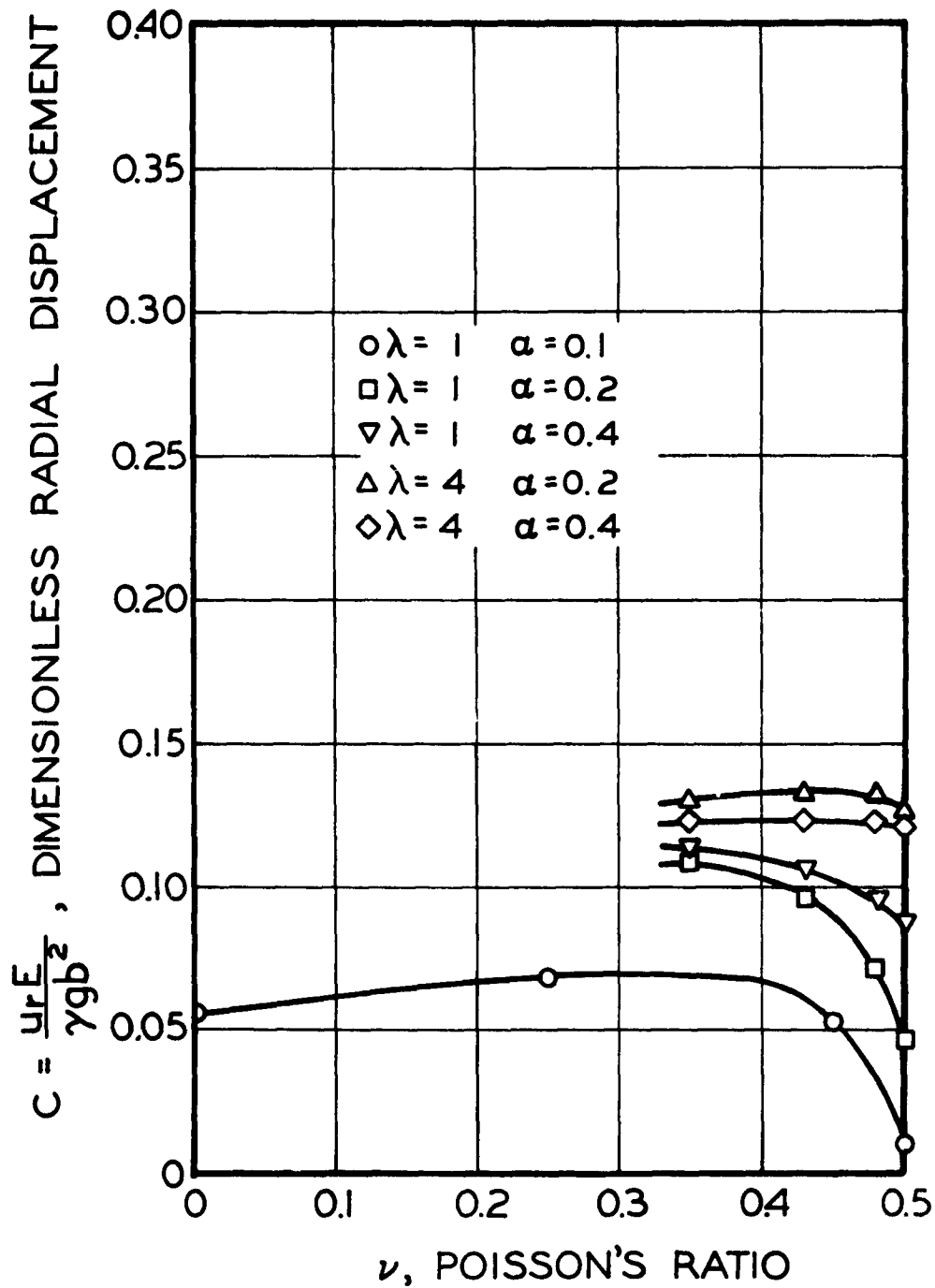
Fig. 28 Radial displacement of free corner of fixed-free cylinder.
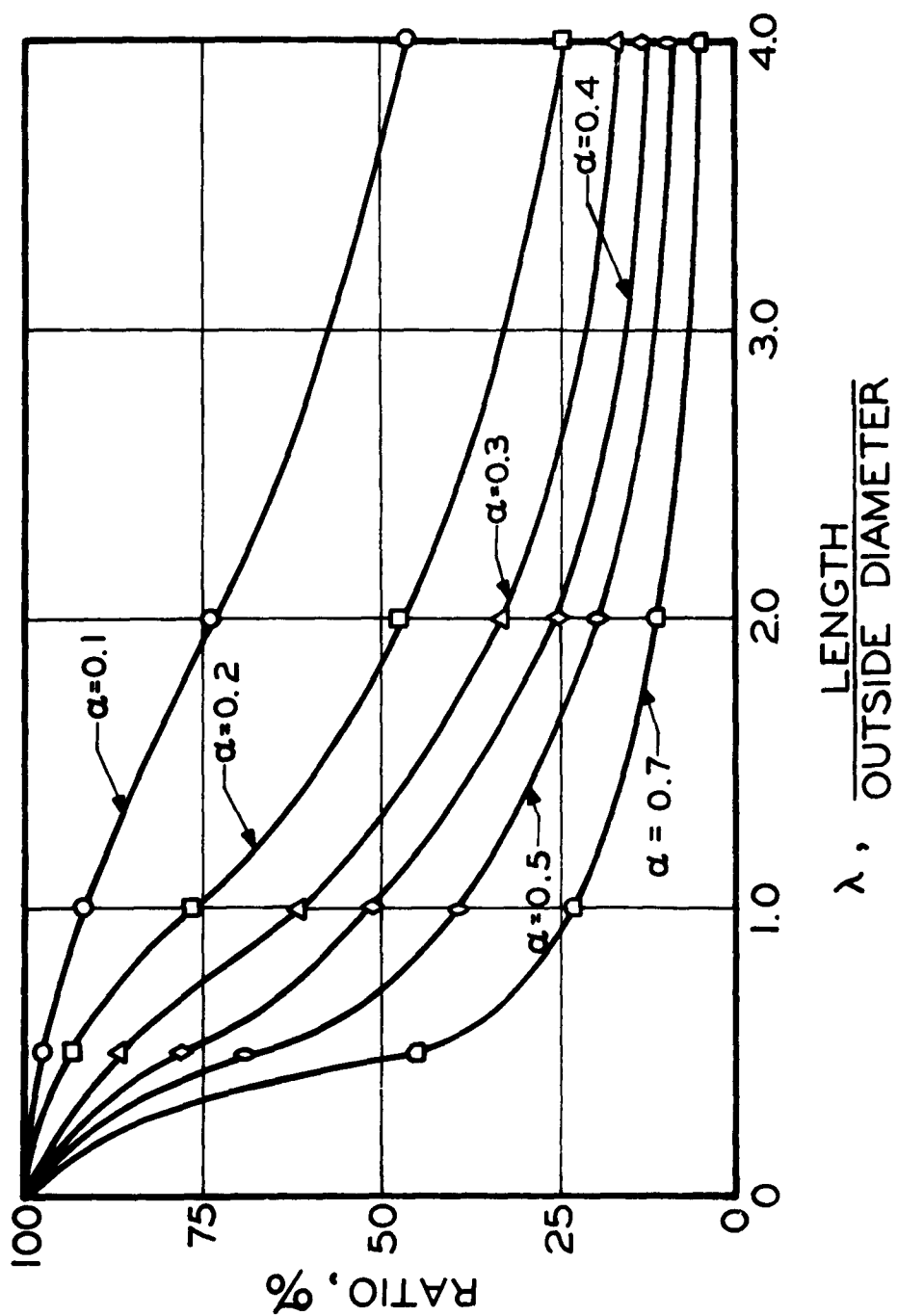
Fig. 29 Ratio of load carried by end bond to total load, $\nu = 0.5$.
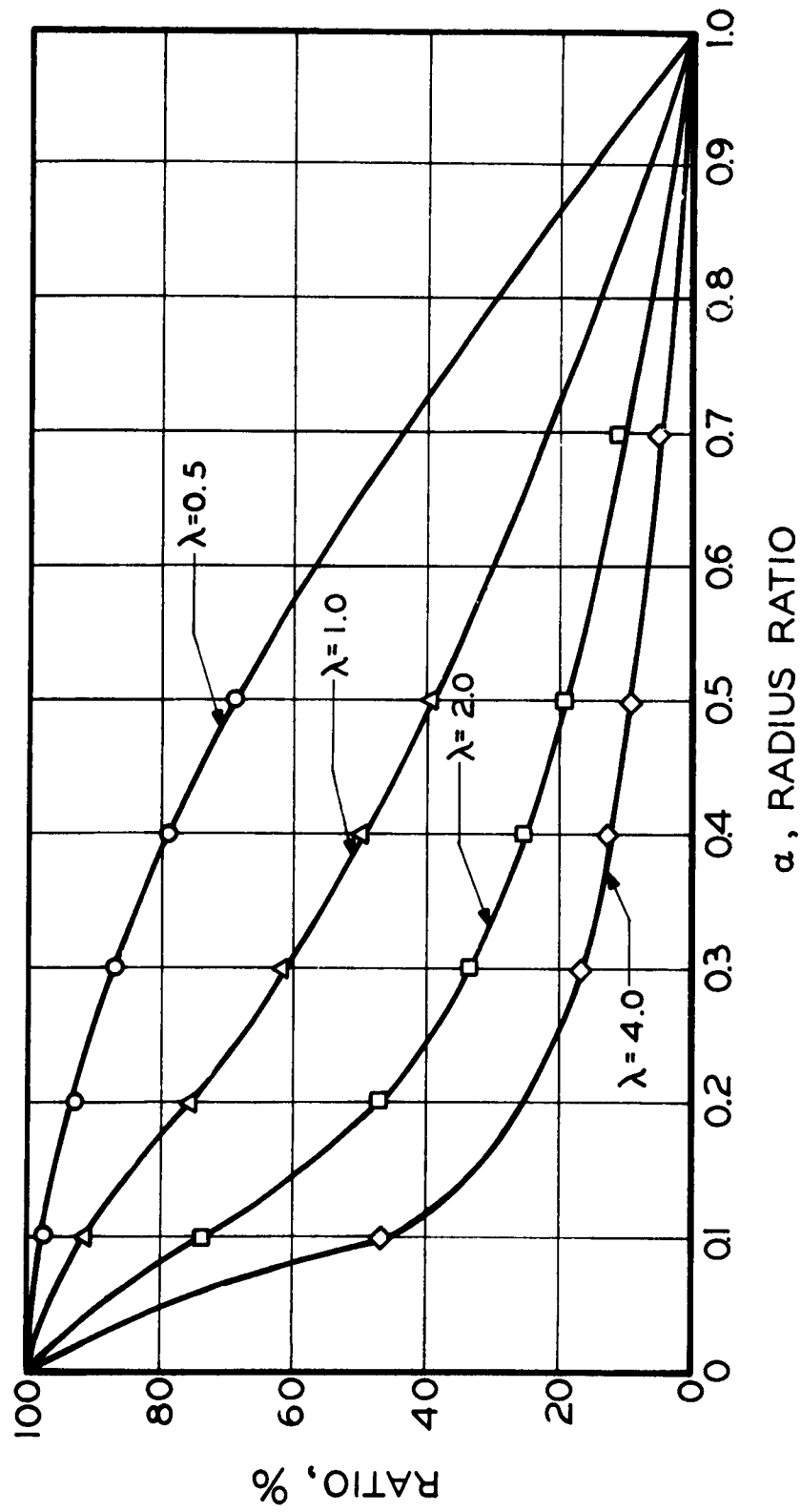
Fig. 30 Ratio of load carried by end bond to total load, ν=0.5.
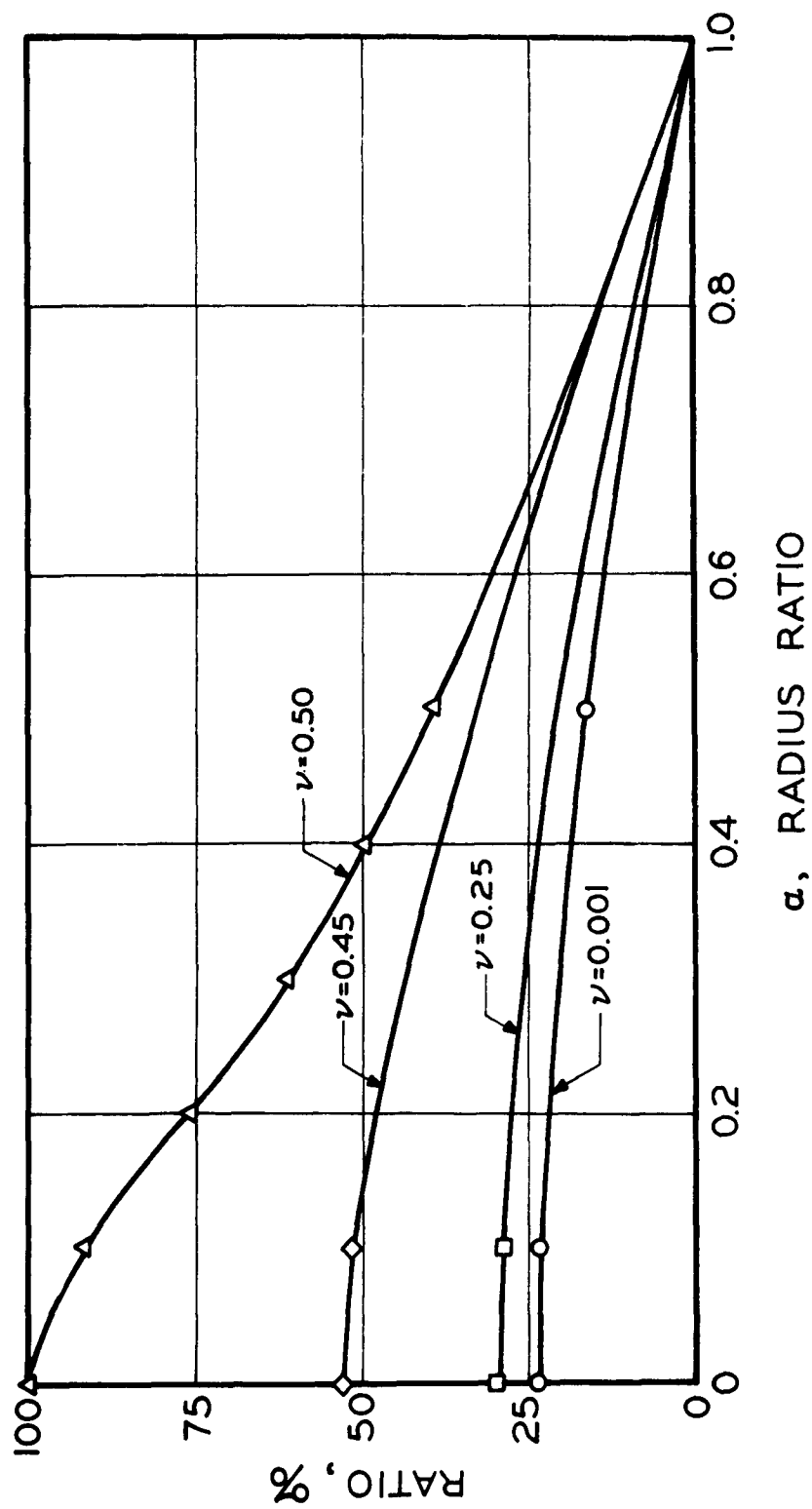
Fig. 31 Ratio of load carried by end bond to total load, $\lambda = 1$.
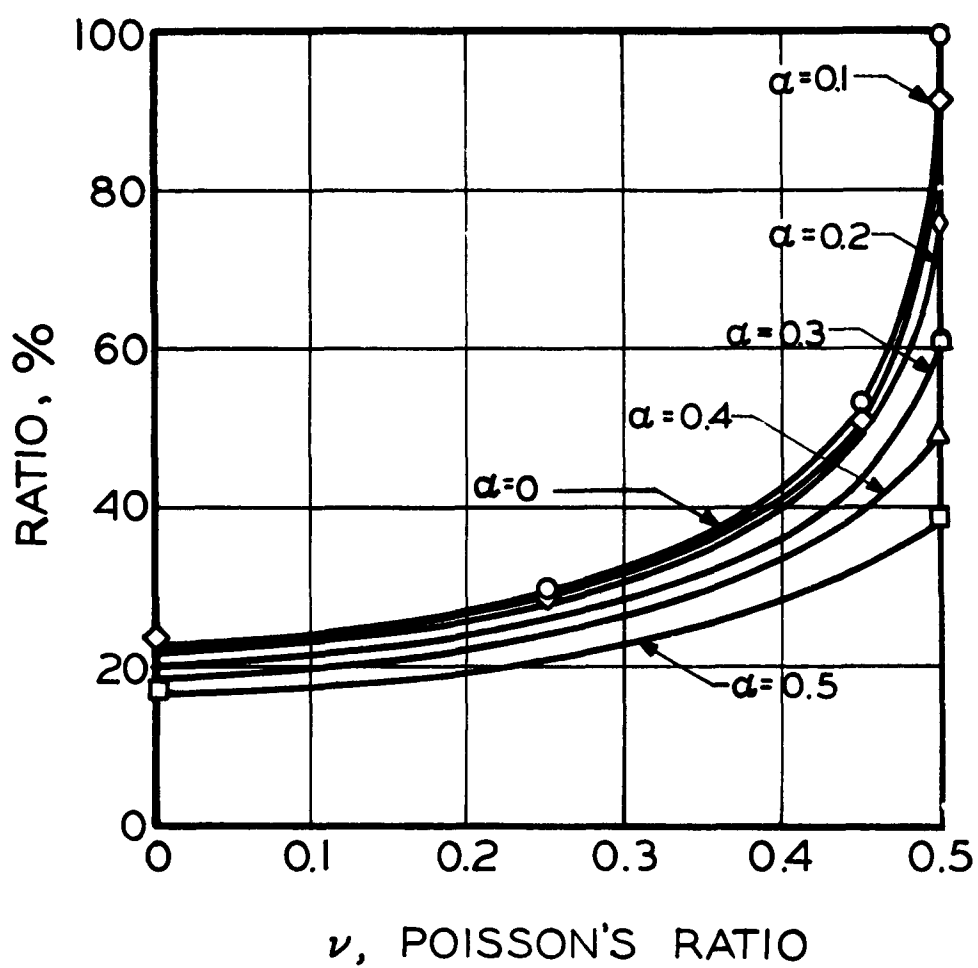
Fig. 32 Ratio of load carried by end bond to total load, λ = 1.
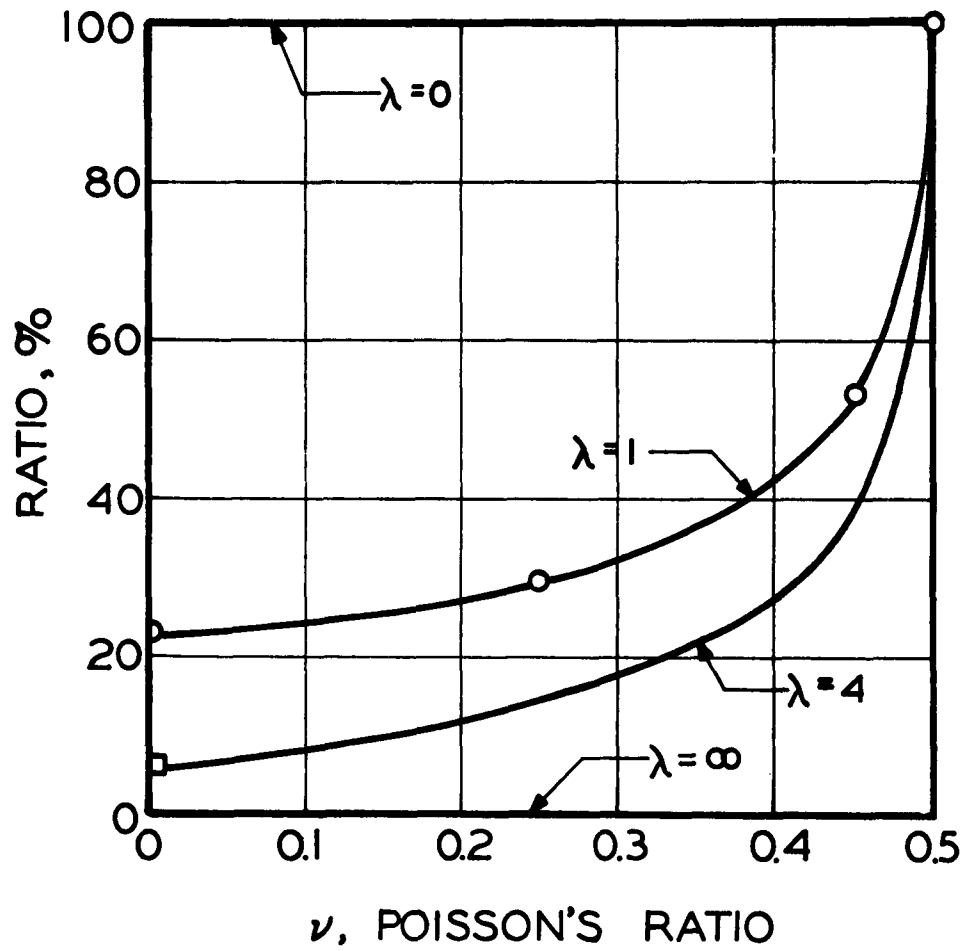
Fig. 33   Ratio of load carried by end bond to total load, a = 0.
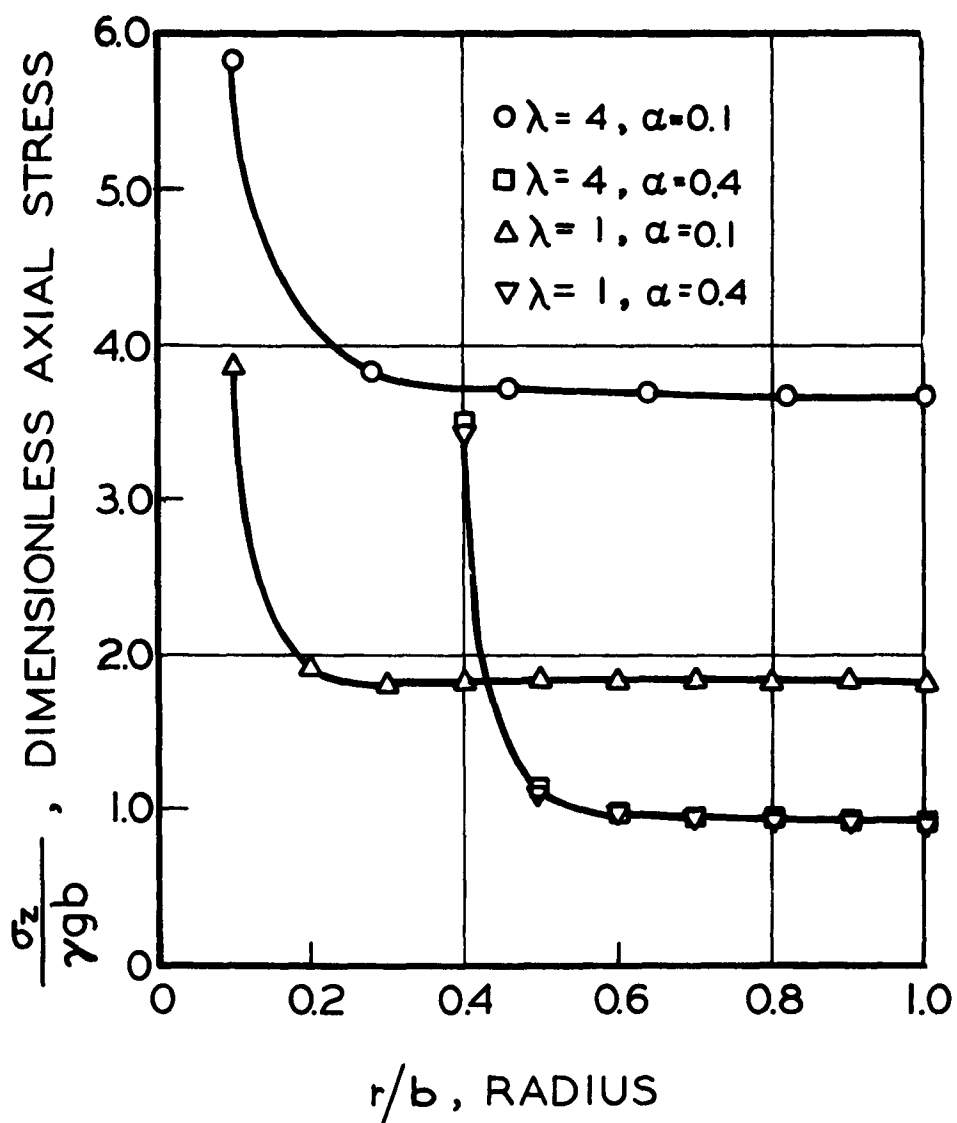
Fig. 34 Distribution of normal stress at head end bond, $\nu = 0.5$.
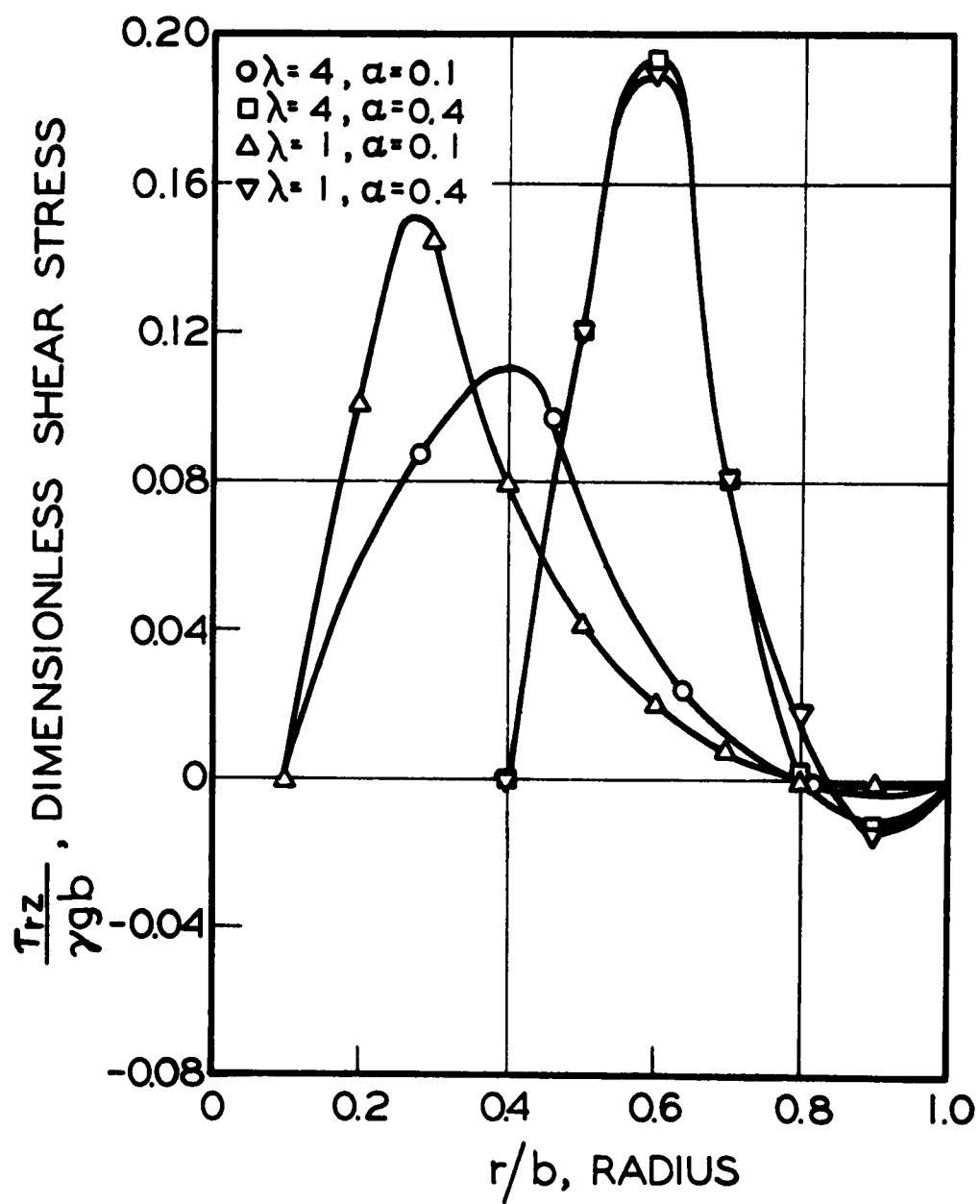
Fig. 35   Distribution of shear stress at head end bond, $\nu = 0.5$.
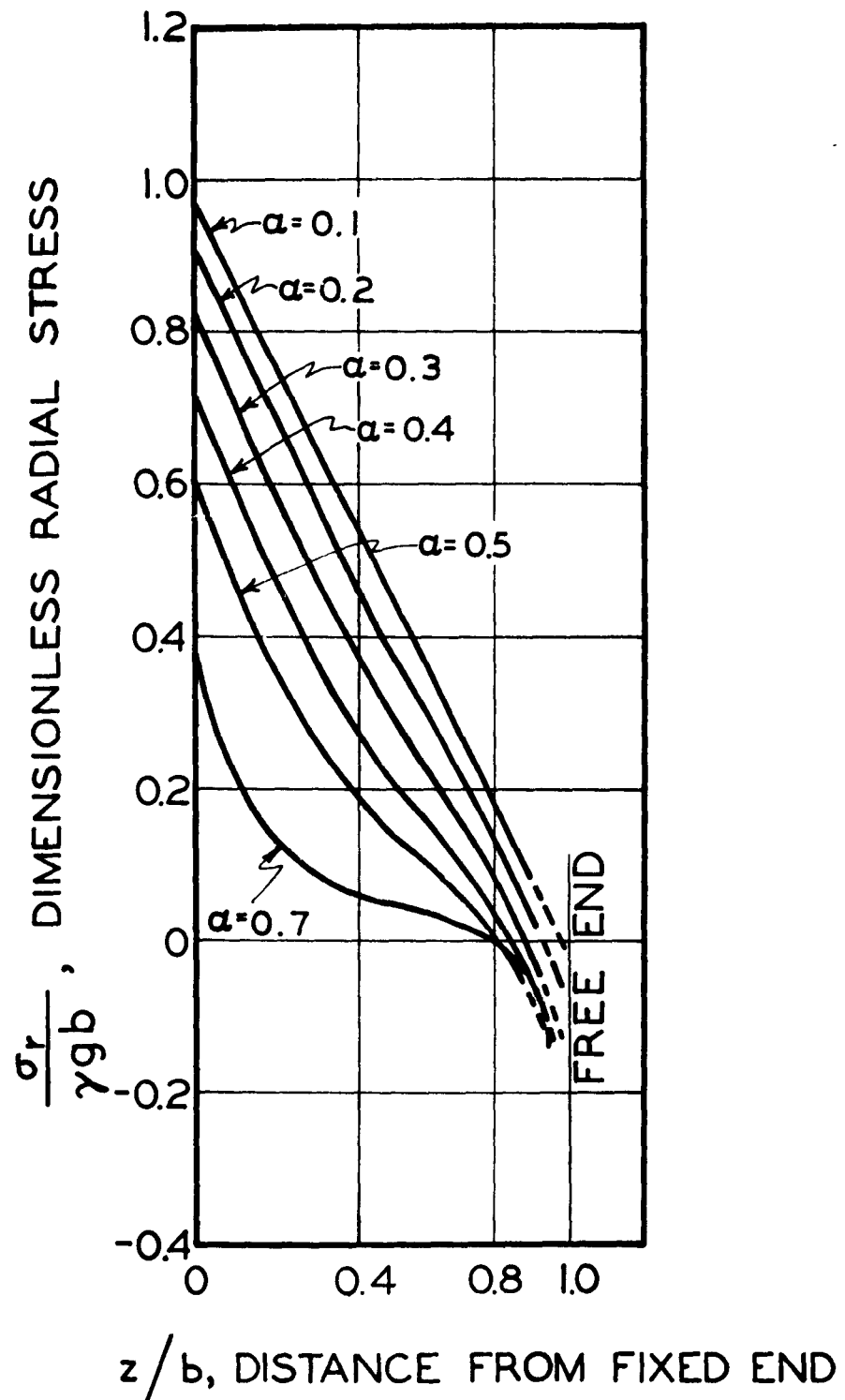
Fig. 36 Dimensionless radial stress at propellant-motor case interface, λ=0.5, ν=0.5.
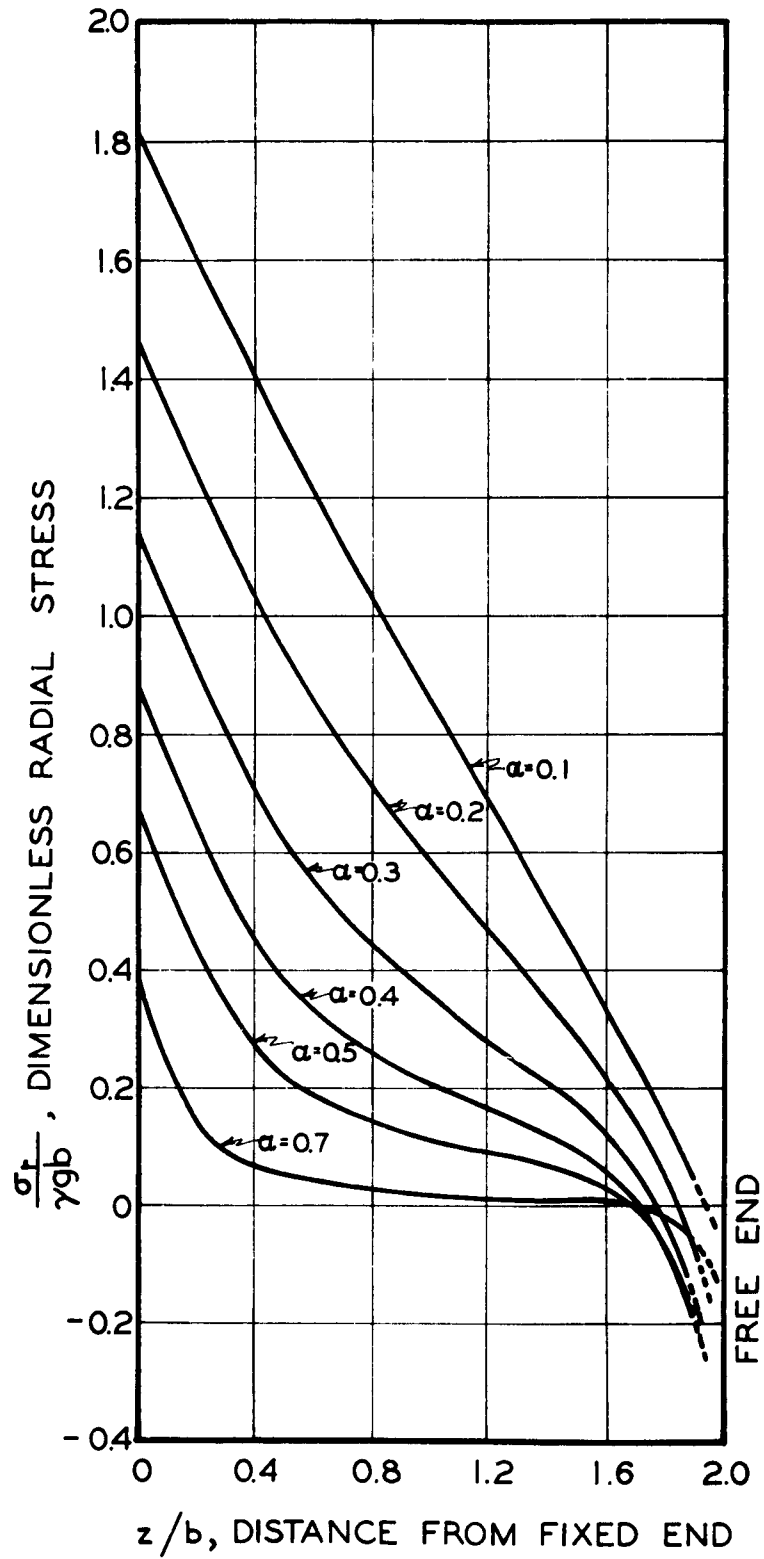
Fig. 37 Dimensionless radial stress at propellant-motor case interface, $\lambda=1$, $\nu=0.5$.
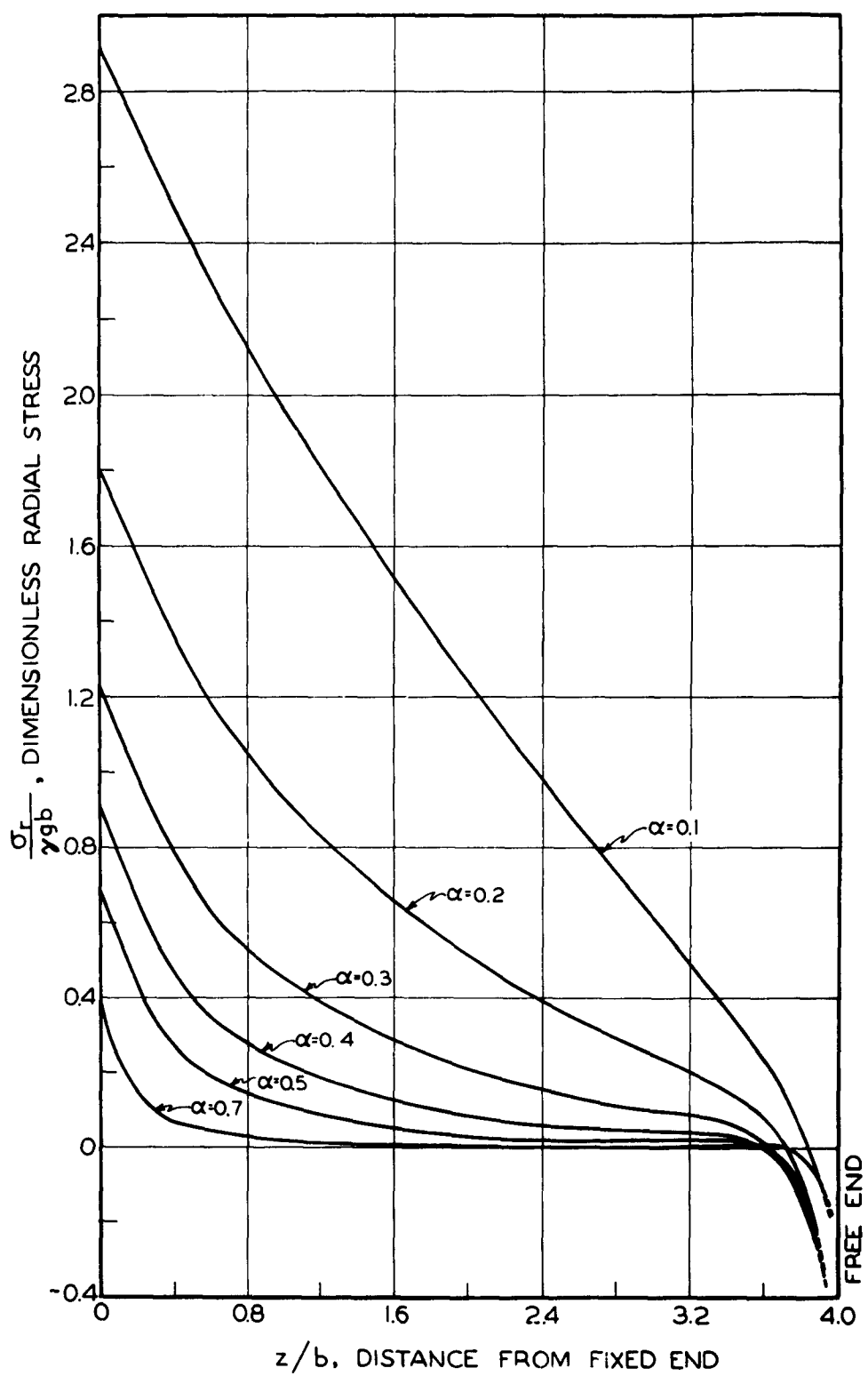
Fig. 38 Dimensionless radial stress at propellant-motor case interface, λ=2, ν=0.5 .
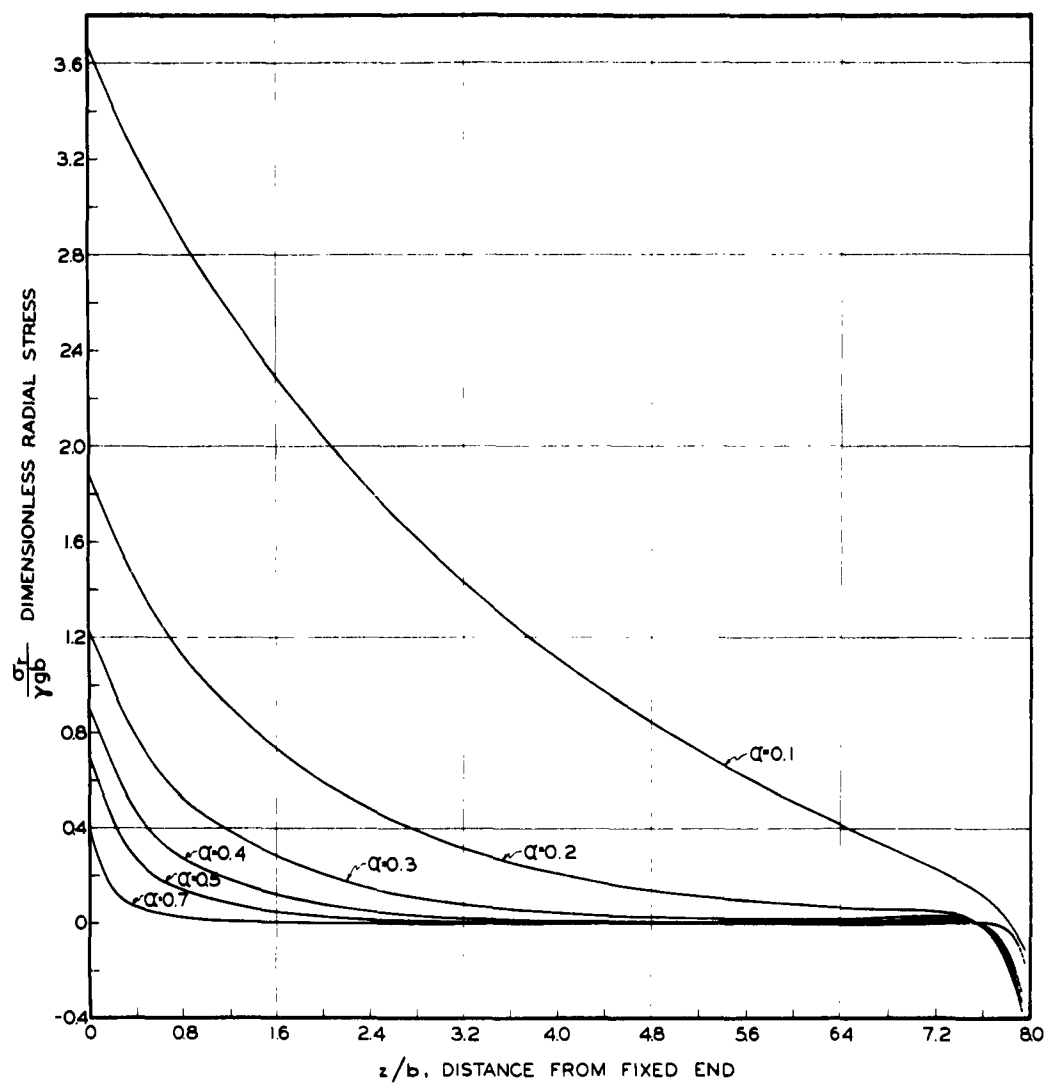
Fig. 39 Dimensionless radial stress at propellant-motor case interface, λ=4, ν=0.5.
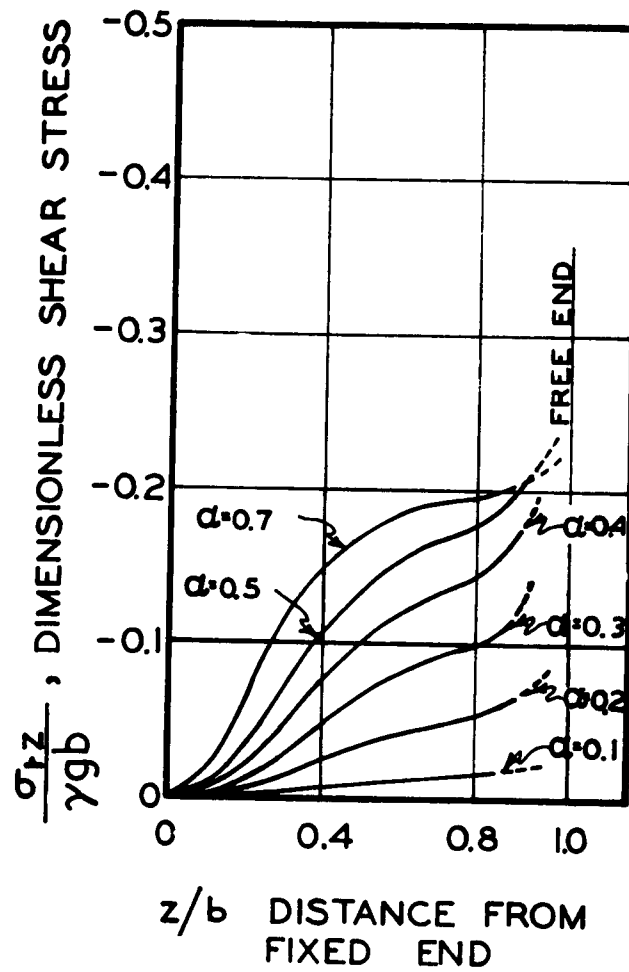
Fig. 40   Dimensionless shear stress at propellant-motor case interface, $\lambda=0.5$, $\nu=0.5$.
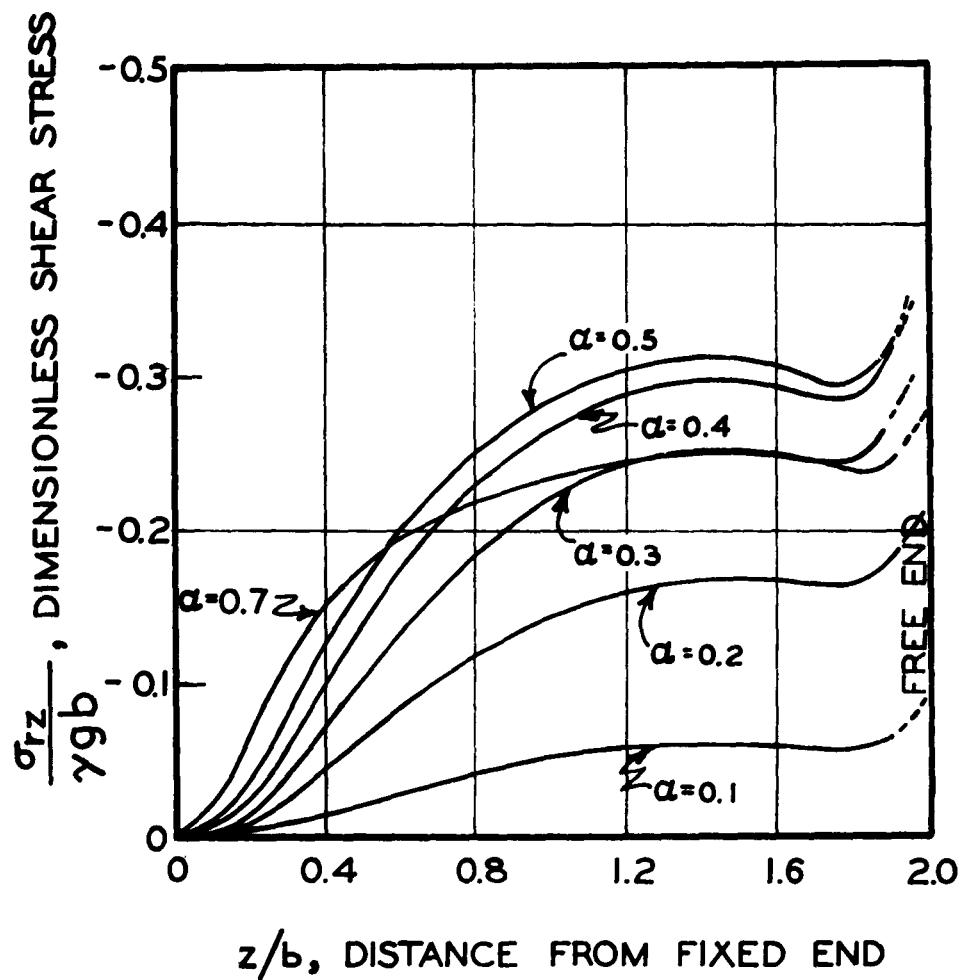
Fig. 41 Dimensionless shear stress at propellant-motor case interface, $\lambda = 1.0$, $\nu = 0.5$.

Fig. 42 Dimensionless shear stress at propellant-motor case interface, $\lambda=2.0$, $\nu=0.5$.
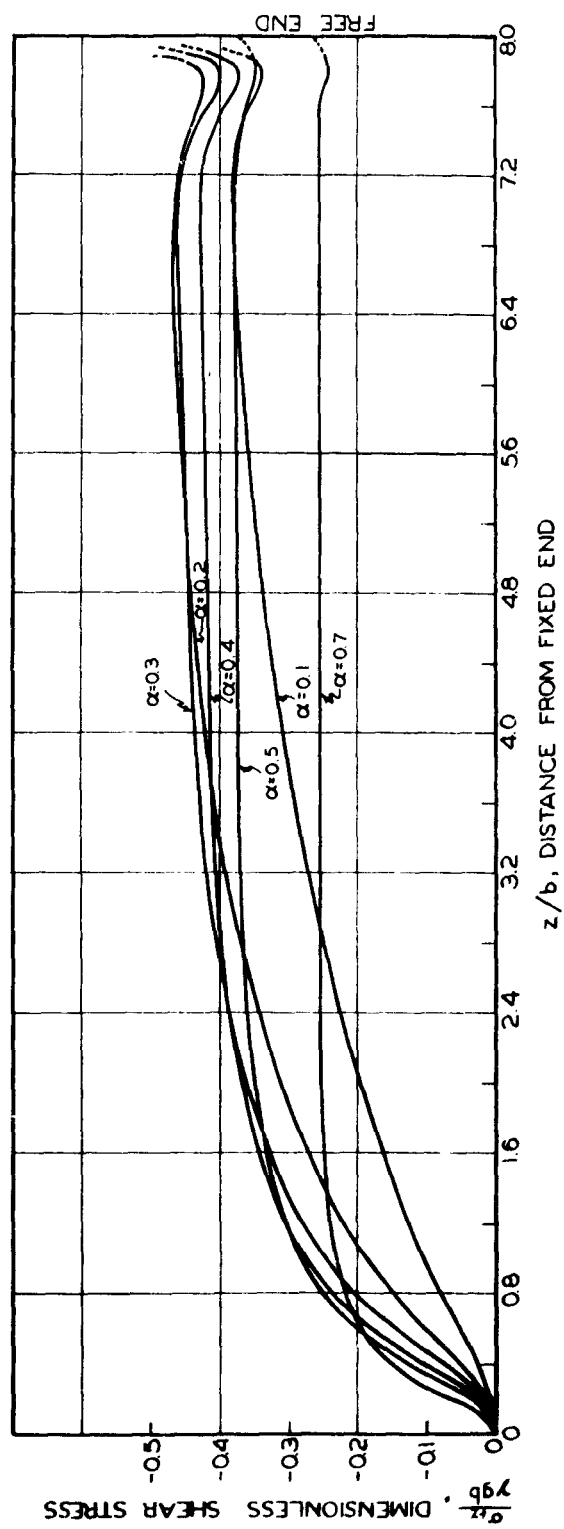
Fig. 43 Dimensionless shear stress at propellant-motor case interface, $\lambda = 4.0$, $\nu = 0.5$.

DEFORMATION OF VISCOELASTIC CYLINDERS OF INFINITE LENGTH AND ARBITRARY CROSS SECTION UNDER AXIAL ACCELERATION LOADS

Charles H. Parr

1. Introduction

A knowledge of the stresses and deformations in solid propellant rocket motors due to axial acceleration loads is necessary for analysis of motor structural integrity. An analysis of the effects of finite length on the stresses and deformations in propellant grains having circular perforations under axial acceleration is presented in another section of this report. This section deals with the axial acceleration of propellant grains of infinite length whose internal perforations are not circular but have a number of axes of symmetry, such as the common types of star perforations.

The equations of motion of a viscoelastic solid were reduced to an uncoupled set by assuming that the deformations do not vary with the coordinate direction along which the acceleration is applied. These results were then applied by the use of conformal mapping to axially accelerated cylinders with cross sections having p axes of symmetry ($p \neq 0$). A closed form solution was obtained for the axial displacement and then evaluated for a particular set of boundary conditions and a particular geometry.

2. Equations of Motion

The equations of motion for a viscoelastic solid may be shown to be[1]

$$\left(K + \frac{G}{3}\right)\left[\frac{\partial\, e(t)}{\partial x}\right] + G\left[\nabla^2 u(t)\right] + X = \gamma\, \frac{\partial^2 u}{\partial t^2} \quad, \tag{1}$$

---

[1]This formulation, with the exception of acceleration and body force terms, has been given by Elder [1].

$$\left(K + \frac{G}{3}\right) \left[\frac{\partial e(t)}{\partial y}\right] + G\left[\nabla^2 v(t)\right] + Y = \gamma \frac{\partial^2 v}{\partial t^2} \quad , \quad \text{and} \qquad (2)$$

$$\left(K + \frac{G}{3}\right) \left[\frac{\partial e(t)}{\partial z}\right] + G\left[\nabla^2 w(t)\right] + Z = \gamma \frac{\partial^2 w}{\partial t^2} \quad , \qquad (3)$$

where the functional notation of Volterra [2]

$$G\left[f(t)\right] = f(t) G(0) + \int_0^t f(t_1) \frac{d}{dt_1} \left[G(t-t_1)\right] dt_1 \qquad (4)$$

is used. Here

G(t) = viscoelastic shear relaxation modulus,

K(t) = viscoelastic bulk relaxation modulus,

u, v, w = displacements in direction of Cartesian coordinates, x, y, z respectively[1],

γ = material density,

t = time,

$$\nabla^2 = \frac{\partial^2}{\partial x^2} + \frac{\partial^2}{\partial y^2} + \frac{\partial^2}{\partial z^2} \quad ,$$

$$e = \frac{\partial u}{\partial x} + \frac{\partial v}{\partial y} + \frac{\partial w}{\partial z} = \text{dilatation, and}$$

X, Y, Z = body forces in the x, y, z, directions, respectively. It should be noted that

$$G\left[\nabla^2 u(t)\right] = \nabla^2 G\left[u(t)\right] \quad . \qquad (5)$$

Under the restriction that u, v, and w are invariant with z, Eqs. 1, 2, and 3 reduce to

---

[1]The displacements u, v, and w are, in general, functions of x, y, and z as well as t. For brevity, the dependence on the coordinates is not expressed in function form but the dependence on t is sometimes expressed to aid in expressing the Volterra and Laplace functionals.

$$\left(K + \frac{G}{3}\right)\left[\frac{\partial^2 u(t)}{\partial x^2} + \frac{\partial^2 v(t)}{\partial x \partial y}\right] + G\left[\frac{\partial^2 u(t)}{\partial x^2} + \frac{\partial^2 u(t)}{\partial y^2}\right] + X = \gamma \frac{\partial^2 u}{\partial t^2} \qquad (6)$$

$$\left(K + \frac{G}{3}\right)\left[\frac{\partial^2 u(t)}{\partial x \partial y} + \frac{\partial^2 v(t)}{\partial y^2}\right] + G\left[\frac{\partial^2 v(t)}{\partial x^2} + \frac{\partial^2 v(t)}{\partial y^2}\right] + Y = \gamma \frac{\partial^2 v}{\partial t^2} , \qquad (7)$$

and

$$G\left[\frac{\partial^2 w(t)}{\partial x^2} + \frac{\partial^2 w(t)}{\partial y^2}\right] + Z = \gamma \frac{\partial^2 w}{\partial t^2} \qquad . \qquad (8)$$

Eqs. 6 and 7 are now uncoupled from Eq. 8. Eqs. 6 and 7 correspond to the usual plane strain equations of viscoelasticity and may be solved separately for any given boundary conditions and body forces. Henceforth, consideration will be given to the solution of Eq. 8 with geometries limited to cylinders having generators parallel to the z-axis. Solutions for the coupled equations, Eqs. 6 and 7, will not be considered in this analysis but can be superposed with solutions of Eq. 8. Note, however, that for a loading of only acceleration in the z-direction, the solution of Eqs. 6 and 7 is trivial, i.e., u = v = 0.

Body forces will be restricted to the weight of the body. It is evident that the weight per unit volume can be expressed as the product of the density γ and a pseudo acceleration, the gravitional constant, and can thus be included in the right side of Eqs. 6, 7, and 8. Consequently the body force will no longer be explicitly considered.

Boundary conditions applicable to Eq. 8 may consist of the specification of the displacement or shear stress as prescribed functions of time. Typically these may take the form

$$w(t) = f(t) \quad \text{on } B_1 \qquad (9)$$

and

$$\tau_{sz}(t) = h(t) \quad \text{on } B_2 \qquad , \qquad (10)$$

where B_1 and B_2 are the boundaries of a hollow cylindrical body and s denotes the normal to the surface.

The displacement w can be considered to consist of two parts, w_1 and w_2, where w_1, a function of time only, is the displacement of boundary B_1 and w_2 is the displacement relative to the boundary B_1. The displacement w_1 may be associated with a rigid body displacement. The displacement w_2 is associated with the deformation of the cylinder material and is a function of the space coordinates x and y and of time t. The displacement w_2 will be further restricted by neglecting dynamic effects so that the magnitude of the variation of w_2 with time is much less than that of w_1. Thus

$$\frac{\partial^2 w}{\partial t^2} \approx \frac{\partial^2 w_1}{\partial t^2} \quad ,$$

and since

$$\frac{\partial w_1}{\partial x} = \frac{\partial w_1}{\partial y} = 0 \quad ,$$

Eq. (8) may be written

$$G\left[\frac{\partial^2 w_2(t)}{\partial x^2} + \frac{\partial^2 w_2(t)}{\partial y^2}\right] = \gamma \frac{\partial^2 w_1(t)}{\partial t^2} \quad . \tag{11}$$

Specification of the overall body acceleration may now be made independently of the displacements associated with deformations.

To obtain a solution to Eq. 11, it is convenient to use the Laplace transform with respect to time to reduce the problem to an associated elastic problem. Applying the Laplace transform to the functional $G\left[w_2(t)\right]$ there results

$$L\left\{G\left[w_2(t)\right]\right\} = G(0)\,\bar{w}_2(p) + \bar{w}_2(p)\left[p\,G(p) - G(0)\right]$$

$$= p\,\bar{w}_2(p)\,\bar{G}(p) \quad , \tag{12}$$

where p is the transform variable, not to be confused with the number p of axes of symmetry of the transverse cross section. Expressing the acceleration of the body as a specified function A(t),

$$\frac{\partial^2 w_1(t)}{\partial t^2} = A(t) \quad , \tag{13}$$

where

$$A(t) = 0, \quad t < 0 \quad ,$$

Eq. 11 becomes

$$\nabla^2 \bar{w}_2(p) = \frac{\gamma \bar{A}(p)}{p \bar{G}(p)} \tag{14}$$

or

$$\nabla^2 \bar{w}_2(p) = \gamma p \bar{A}(p) \bar{J}(p) \tag{15}$$

since

$$p \bar{G}(p) = \frac{1}{p \bar{J}(p)} \quad ,$$

where $\bar{J}(p)$ is the Laplace transform of the shear compliance. Taking the inverse Laplace transform, there results

$$\nabla^2 L^{-1} \left\{ \bar{w}_2(p) \right\} = L^{-1} \left\{ \gamma p \bar{A}(p) \bar{J}(p) \right\} \quad , \tag{16}$$

where $L^{-1} \left\{ \ \right\}$ denotes the inverse Laplace transform. Letting

$$\psi = \frac{L^{-1} \left\{ \bar{w}_2(p) \right\}}{L^{-1} \left\{ \gamma p \bar{J}(p) \bar{A}(p) \right\}} \quad , \tag{17}$$

Eq. 16 becomes

$$\frac{\partial^2 \psi}{\partial x^2} + \frac{\partial^2 \psi}{\partial y^2} = 1 \quad . \tag{18}$$

Note that ψ is a function of x and y only and is not a function of time. Eq. 18 is valid regardless of the time dependence of the acceleration and regardless of the time dependence of the shear compliance. Further it can be seen from Eq. 18 that the displacement function ψ defined by Eq. 17 depends solely on the space coordinates x, y and the boundary conditions.

If the acceleration A(t) is applied as a step function,

$$A(t) = g H(t) \quad ,$$

where H(t) is the unit step function and g is a constant, then
$\overline{A}(p) = g/p$, and

$$\psi = \frac{L^{-1}\left\{\overline{w}_2(p)\right\}}{L^{-1}\left\{g \gamma \overline{J}(p)\right\}} = \frac{w_2(t)}{g \gamma J(t)} \quad . \tag{19}$$

Thus for a step function in the acceleration, the axial displacement
at each point is directly proportional to the creep compliance.

3. Application to Star Geometries

The solution of Poisson's equation, Eq. 18, was con-
sidered for star geometries which are applicable to solid propellant
grains. Consider the shape shown in Fig. 1. The internal perforation
consists of p branches or star points and the external boundary is
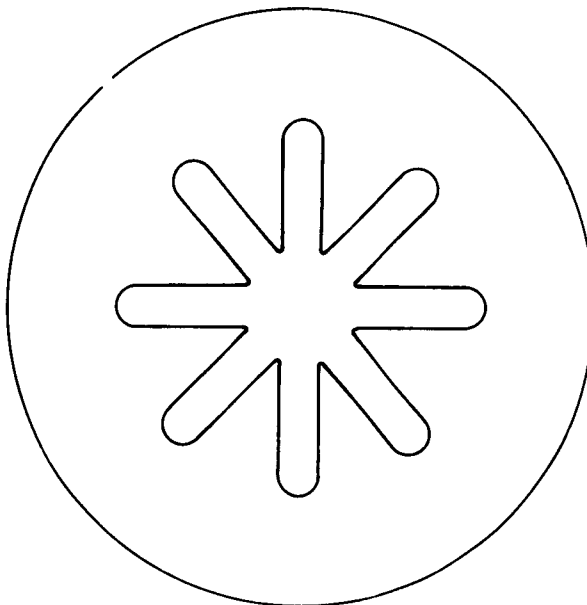circular. Wilson [3, 4] demonstrated the mapping of such regions by

Fig. 1 Typical star perforated propellant grain.

fitting the internal perforation with a mapping transform which maps the star shape in the z* or real plane[1] onto the unit circle in the ζ or transformed plane. Likewise, the circle defined by $\rho = \Gamma$ in the ζ plane corresponds to an irregular line in the z* plane. However, if Γ is sufficiently large the corresponding contour in the z*-plane is sufficiently regular to be considered circular.

The mapping function used by Wilson is given by

$$z^* = \omega(\zeta) = A\zeta + \frac{B}{\zeta^{p-1}} + \frac{C}{\zeta^{2p-1}} + \frac{D}{\zeta^{3p-1}} + \cdots , \tag{20}$$

where p is the number of axes of symmetry of the grain cross section. Kantorovich and Krylov [5] show that under such a transformation, the Laplace operator transforms into

$$\left(\frac{\partial^2}{\partial x^2} + \frac{\partial^2}{\partial x^2} \right) = \frac{1}{|\omega'(\zeta)|^2} \left(\frac{\partial^2}{\partial \xi^2} + \frac{\partial^2}{\partial \eta^2} \right) , \tag{21}$$

where $\omega'(\zeta)$ is the derivative of ω with respect to ζ. Expressing Eq. 21 in polar coordinates by means of

$$\zeta = \xi + i\eta = \rho e^{i\theta} ,$$

the Laplace operator becomes

$$\left(\frac{\partial^2}{\partial x^2} + \frac{\partial^2}{\partial y^2} \right) = \frac{1}{|\omega'(\zeta)|^2} \left(\frac{\partial^2}{\partial \rho^2} + \frac{1}{\rho} \frac{\partial}{\partial \rho} + \frac{1}{\rho^2} \frac{\partial^2}{\partial \theta^2} \right) . \tag{22}$$

Using Eq. 22, Eq. 18 may be written

$$\frac{\partial^2 \psi}{\partial \rho^2} + \frac{1}{\rho} \frac{\partial \psi}{\partial \rho} + \frac{1}{\rho^2} \frac{\partial^2 \psi}{\partial \theta^2} = |\omega'(\zeta)|^2 . \tag{23}$$

Now consider the general form of $\omega(\zeta)$,

---

[1]To avoid confusion with the z coordinate, an asterisk is used to denote the complex variable $z^* = x + iy$.

$$\omega(\zeta) = \sum_0^N C_n \zeta^{1-np} \quad . \tag{24}$$

Then

$$\omega'(\zeta) = \sum_0^N (1-np) C_n \zeta^{-np}$$

or

$$\omega'(\zeta) = \sum_0^N \frac{(1-np) C_n}{\rho^{np}} \left[\cos np\theta - i \sin np\theta \right] \quad . \tag{25}$$

Then

$$|\omega'(\zeta)|^2 = \left[\sum_0^N \frac{(1-np) C_n}{\rho^{np}} \cos np\theta \right]^2$$

$$+ \left[\sum_0^N \frac{(1-np) C_n}{\rho^{np}} \sin np\theta \right]^2 \quad , \tag{26}$$

or, upon expanding,

$$|\omega'(\zeta)|^2 = \sum_{n=0}^N \sum_{m=0}^N \frac{(1-np)(1-mp) C_n C_m}{\rho^{(m+n)p}} \cos mp\theta \cos np\theta$$

$$+ \sum_{n=0}^N \sum_{m=0}^N \frac{(1-np)(1-mp) C_n C_m}{\rho^{(m+n)p}} \sin mp\theta \sin np\theta \quad , \tag{27}$$

which simplifies to

$$| \omega'(\zeta) |^2 = \sum_{n=0}^{N} \sum_{m=0}^{N} \frac{(1-np)(1-mp) C_n C_m}{\rho^{(m+n)p}} \cos(m-n)p\theta \quad . \tag{28}$$

Let $k = m-n$. Then, after considerable manipulation, Eq. 28 may be rewritten in the form

$$| \omega'(\zeta) |^2 = \sum_{n=0}^{N} \frac{(1-np)^2 C_n^2}{\rho^{2np}}$$

$$+ 2 \sum_{k=1}^{N} \left[\cos kp\theta \sum_{n=0}^{N-k} \frac{(1-np)(1-np-kp) C_n C_{n+k}}{\rho^{(2n+k)p}} \right] . \tag{29}$$

The solutions to Laplace's equation which will form the complementary part of the solution to Eq. 23 are well known[1]. Those forms suitable for the problem under discussion are

$$\psi_1 = \sum_{k=1}^{N} (H_k \rho^{kp} + L_k \rho^{-kp}) \cos kp\theta + U \ln \rho + V \quad , \tag{30}$$

where H_k, L_k, U, and V are to be determined from the boundary conditions.

The particular solution of Eq. 23 may be found by considering

$$\psi_2 = M_{nk} \rho^{\alpha} \cos kp\theta \quad . \tag{31}$$

Substituting this relation together with Eq. 29 into Eq. 23 and equating coefficients of $\cos kp\theta$ results in

---

[1]See, for instance, Moon and Spencer [6], p. 14.

$$\alpha = 2 - (2n + k)p \quad ,$$

$$M_{nk} = \frac{C_n C_{n+k}}{2} \quad , \qquad k \neq 0 \quad , \tag{32}$$

and

$$M_{n0} = \frac{C_n^2}{4} \quad .$$

The particular solution is then formed by a double series in n and k of terms given by Eq. 31.

The complete solution is then given by adding the complementary and particular solutions which results in

$$\psi = \sum_{n=0}^{N} \frac{C_n^2}{4} \rho^{2(1-np)} + U \ln \rho + V$$

$$+ \sum_{k=1}^{N} \left\{ H_k \rho^{kp} + L_k \rho^{-kp} + \sum_{n=0}^{N-k} \frac{C_n C_{n+k}}{2} \rho^{2-(2n+k)p} \right\} \cos kp\theta \quad . \tag{33}$$

This is the solution for the axial displacement function ψ in an infinite cylinder whose contour in the transverse cross section can be defined by a mapping function of the form Eq. 20 (or Eq. 24) .

4. <u>Satisfaction of Boundary Conditions</u>

Consider the boundary conditions

$$w(x, y, t) = w_1(t) + w_2(x, y, t) = f(t) \qquad \text{on } B_1 \tag{9}$$

and

$$\tau_{sz} = h(t) \qquad \text{on } B_2 \quad , \tag{10}$$

By definition

$$w_2(B_1, t) = 0 \quad , \tag{34}$$

so that the first boundary condition, Eq. 9, can be written

$$w(x, y, t) = w_1(t) = f(t) = \iint A(t) \, dt \, dt \qquad \text{on } B_1 \quad . \tag{35}$$

Considering the second boundary condition, Eq. 10, where s is the outward normal, the shear stress can be expressed in terms of shear strain and, in turn, in terms of the axial displacement w_2 and normal displacement u_s resulting in

$$\tau_{sz} = G\left[\gamma_{sz}(t)\right] = G\left[\frac{\partial u_s(t)}{\partial z} + \frac{\partial w_2(t)}{\partial s}\right] = G\left[\frac{\partial w_2(t)}{\partial s}\right] \quad . \tag{36}$$

Taking $h(t) = 0$, boundary condition Eq. 10 thus reduces to

$$G\left[\frac{\partial w_2(t)}{\partial s}\right] = 0 \qquad \text{on } B_2 \quad . \tag{37}$$

Eq. 37 is a homogeneous Volterra integral equation and the only continuous solution is zero [7]. Thus

$$\frac{\partial w_2}{\partial s} = 0 \quad . \tag{38}$$

For the mapping function used, it can be shown that

$$\frac{\partial}{\partial s} = -\frac{1}{|\omega'(\zeta)|} \frac{\partial}{\partial \rho} \tag{39}$$

on an internal boundary and

$$\frac{\partial}{\partial s} = \frac{1}{|\omega'(\zeta)|} \frac{\partial}{\partial \rho} \tag{40}$$

on an external boundary.

Defining B_1 as the outer boundary and B_2 as the inner boundary, the boundary conditions in the transformed plane, with the use of Eqs. 34, 38, and 39, become

$$w_2(t) = 0 \qquad \text{on } B_1 \tag{41}$$

and

$$\frac{\partial w_2(t)}{\partial \rho} = 0 \qquad \text{on } B_2 \quad . \tag{42}$$

Since these conditions are independent of time they may be applied
directly to the function ψ to yield

$$\psi = 0 \qquad \text{on } B_1 \tag{43}$$

and

$$\frac{\partial \psi}{\partial \rho} = 0 \qquad \text{on } B_2 \quad . \tag{44}$$

Letting

$$\rho = 1 \qquad \text{on } B_1$$

and

$$\rho = \beta \qquad \text{on } B_2 \quad ,$$

the unknowns H_k, L_k, U, and V in Eq. 33 can be evaluated with the
aid of Eqs. 43 and 44 allowing Eq. 33 to be written as

$$\psi = \sum_{n=0}^{N} \frac{C_n^2}{4} \left\{ \rho^{2(1-np)} - \beta^{2(1-np)} - 2(1-np)\ln\left|\frac{\rho}{\beta}\right| \right\}$$

$$+ \sum_{k=1}^{N} \left\{ \sum_{n=0}^{N-k} \frac{C_n C_{n+k}}{2} \left[\rho^{2(1-np)} - \beta^{2(1-np)} \right. \right.$$

$$\left. \left. + \frac{\left|\dfrac{2-np-kp}{kp} + \beta^{2(1-np)}\right| \left|\beta^{2kp} - \rho^{2kp}\right|}{1 + \beta^{2kp}} \right] \right\} \rho^{-kp} \cos kp\theta \;. \tag{45}$$

5. Evaluation of Displacements and Shear Stresses

Due to the form of the mapping function $\omega(\zeta)$, Eq. 24,
an inverse is not easily obtainable. Thus the value of $\zeta = \rho\, e^{i\theta}$
corresponding to a given location $z^* = x + i\,y$ cannot be explicitly
obtained but must be approximated. A straightforward way of evalu-
ating the expression for displacement is to perform the evaluation
of ψ and z^* for a series of ρ's and θ's and then use interpolation to
obtain values of displacement at specific values of z. In this manner

the dimensionless displacement ψ can be evaluated at any point for a given geometry from Eq. 45 by specifying the C_n and β. The actual time-dependent displacement w_2 can then be obtained by performing the operations indicated by Eq. 17 once the acceleration $A(t)$ and the creep compliance $J(t)$ are specified.

The shear stress is somewhat more difficult to evaluate. Since the displacements u and v in the x - y plane are zero for a loading of axial acceleration, the shear stresses due to the axial acceleration load are given by

$$\tau_{\ell z} = G\left[\frac{\partial w(t)}{\partial \ell}\right] \quad , \tag{46}$$

where ℓ is any desired line lying in the z^* or x - y plane. Taking the Laplace transform of this expression with respect to time,

$$\overline{\tau}_{\ell z}(p) = p\, \overline{G}(p)\, \frac{\partial \overline{w}(p)}{\partial \ell} \quad , \tag{47}$$

the transformed shear stress can be written, with the use of Eq. 17, as

$$\overline{\tau}_{\ell z}(p) = \gamma\, \overline{A}(p)\, \frac{\partial \psi}{\partial \ell}$$

or simply

$$\tau_{\ell z} = \gamma\, A(t)\, \frac{\partial \psi}{\partial \ell} \quad . \tag{48}$$

Usually the maximum values of shear stress at a point are wanted. These may be obtained in the following manner. The relation of the derivative along a line ℓ in z^*-plane to the derivative along a corresponding line λ in the ζ-plane is given by

$$\frac{\partial \psi}{\partial \ell} = \frac{1}{|\omega'(\zeta)|}\, \frac{\partial \psi}{\partial \lambda} \quad . \tag{49}$$

In terms of the ρ-θ coordinates

$$\frac{\partial \psi}{\partial \lambda} = \frac{\partial \psi}{\partial \rho}\, \frac{\partial \rho}{\partial \lambda} + \frac{\partial \psi}{\partial(\rho\theta)}\, \frac{\partial(\rho\theta)}{\partial \lambda} \quad . \tag{50}$$

But

$$\frac{\partial \rho}{\partial \lambda} = \cos \alpha \tag{51}$$

and

$$\frac{\partial (\rho \theta)}{\partial \lambda} = \sin \alpha \quad , \tag{52}$$

where α is the angle between λ and the ρ coordinate line. Substituting Eq. 51 and Eq. 52 in Eq. 50 and maximizing with respect to α, there results

$$\frac{\partial \psi}{\partial \lambda} \bigg|_{max} = \sqrt{\left|\frac{\partial \psi}{\partial \rho}\right|^2 + \frac{1}{\rho^2} \left|\frac{\partial \psi}{\partial \theta}\right|^2} \quad . \tag{53}$$

Eqs. 48, 49, and 53 yield

$$\tau_{max} = \gamma A(t) \sqrt{\frac{\left|\frac{\partial \psi}{\partial \rho}\right|^2 + \frac{1}{\rho^2} \left|\frac{\partial \psi}{\partial \theta}\right|^2}{|\omega'(\zeta)|^2}} \quad .$$

The displacement function ψ has been evaluated for the six-point, star-perforated shape shown in Fig. 2 which has been mapped with a 50 term mapping function. The original ballistic configuration is indicated by the dashed lines. The curvilinear coordinates are shown over a part of the cross section, demonstrating the slight mismatch between the true circular outer boundary and the curvilinear coordinate. A contour map of the displacement is shown in Fig. 3 for a step-function acceleration load, i.e., $A(t) = g H(t)$.

6. **References**

1. Elder, A.S., "General Solution of Certain Integro-Differential Equations of Linear Viscoelasticity", 20th Meeting Bulletin of the JANAF-ARPA-NASA Panel on Physical Properties of Solid Propellants (1961), Vol. 1, p. 31.

2. Volterra, Vito, "Theory of Functional and of Integral and Integro-Differential Equations", Dover Publications, New York (1959).

3. Wilson, H.B., Jr., "Conformal Transformation of a Solid
    Propellant Grain with a Star Shaped Internal Perforation
    Onto an Annulus", ARS Journal, 30, 780 (1960).

4. Wilson, H.B., Jr., "A Method of Conformal Mapping and
    the Determination of Stresses in Solid Propellant Rocket
    Grains", Rohm & Haas Company, Report No. S-38,
    April 1963.

5. Kantorovich, L.V., and Krylov, V.I., "Approximate Methods
    of Higher Analysis", translated by C. Benster, Interscience,
    New York, 1958.

6. Moon, Parry, and Spencer, D.E., "Field Theory Handbook",
    Springer-Verlag, Berlin, 1961.

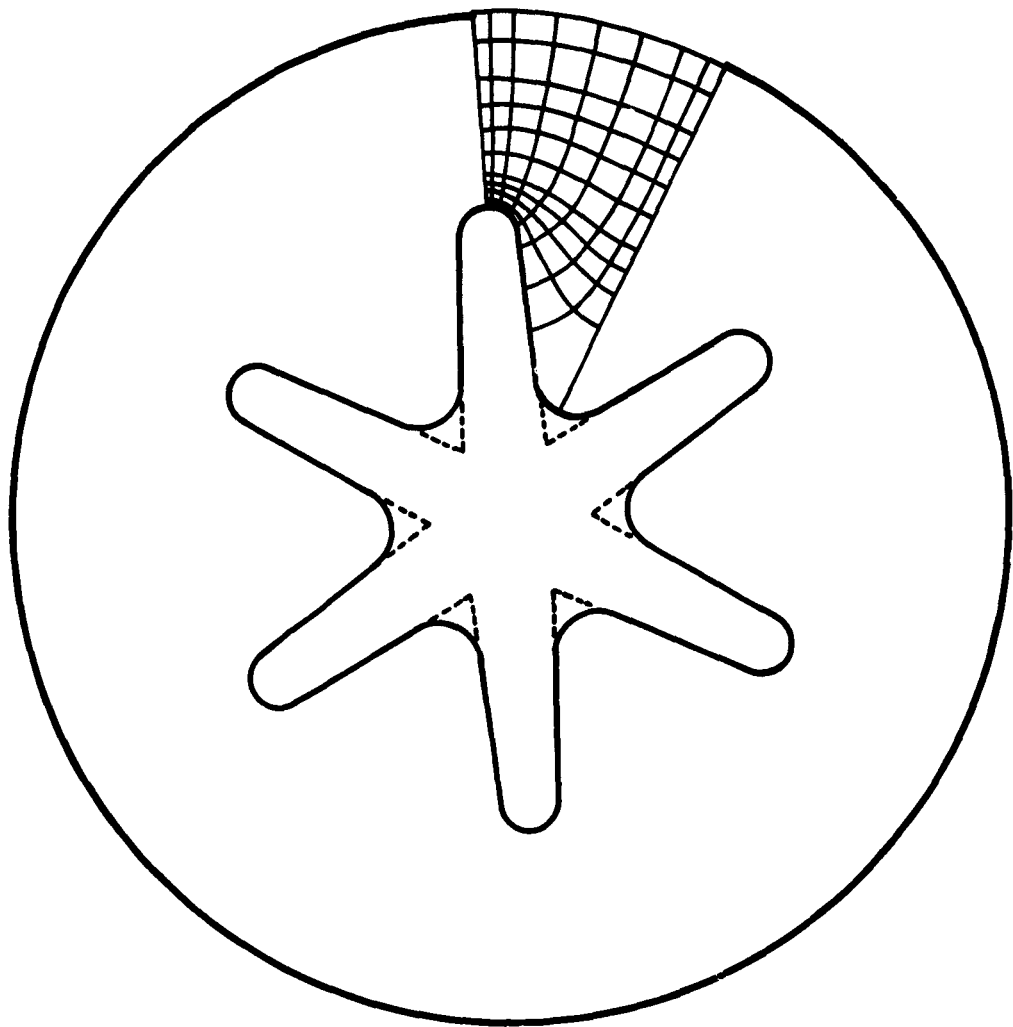7. Tricomi, F.G., "Integral Equations" Interscience, New
    York, 1959.

Fig. 2 Curvilinear coordinates obtained by conformal mapping.
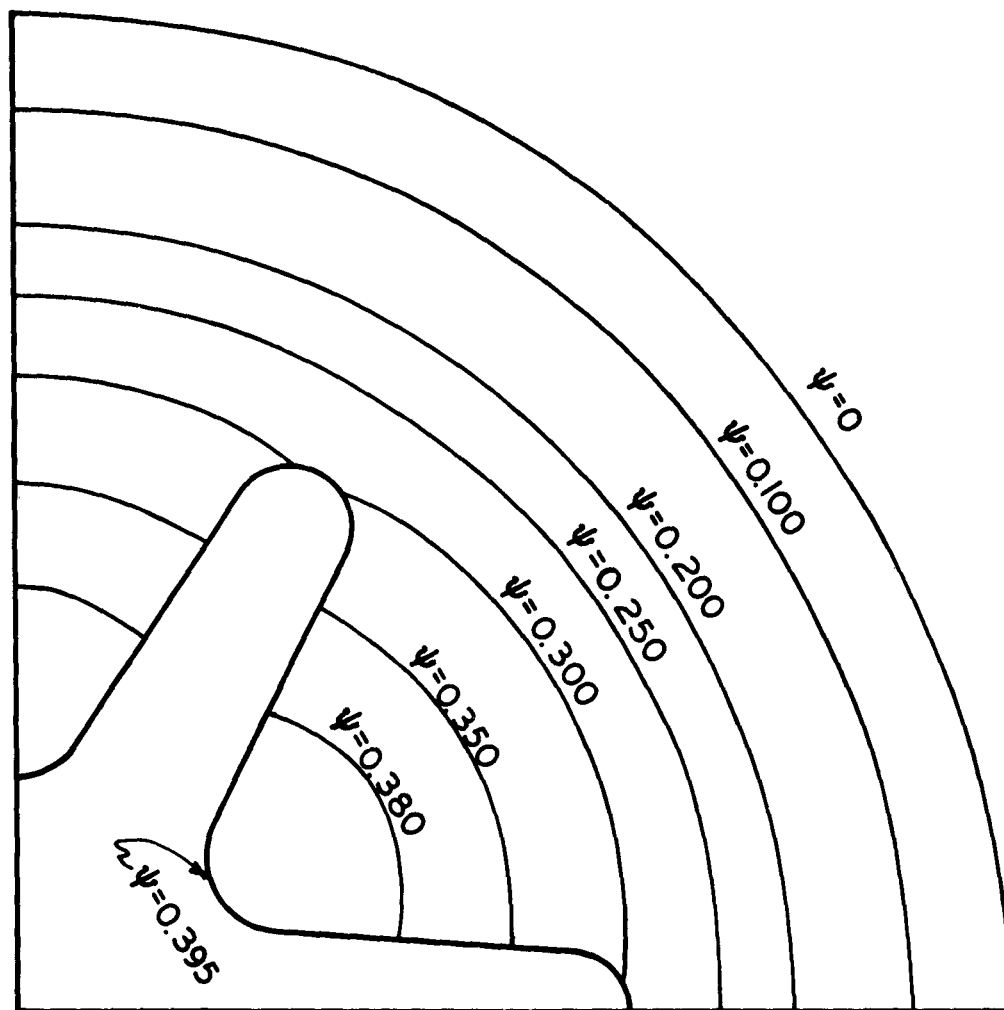
Fig. 3 Contour map of displacement function ψ.

Initial distribution of this report was made
in accordance with the Joint Army-Navy-
Air Force mailing lists for Solid Propellant
and Liquid Propellant technical information
plus approved supplements